Dalton Transactions

ROYAL SOCIETY OF CHEMISTRY

PAPER

View Article Online
View Journal | View Issue

Check for updates

Cite this: *Dalton Trans.*, 2025, **54**, 15235

C_2-Symmetric Ru(II) bimetallic complex catalysed selective degradation and value addition of azo dyes

Gopal Deshmukh, Thakur Rochak Kumar Rana, Neha Yadav, Gopalan Rajaraman * and Ramaswamy Murugavel *

Received 30th July 2025,
Accepted 4th September 2025

DOI: 10.1039/d5dt01813g

rsc.li/dalton

The textile industry pollutes water with persistent azo dyes, yet their complete hydrogenation remains underexplored. Herein, we report for the first time the use of bimetallic Ru(II) complexes for catalytic azo bond activation, achieving complete degradation in both aqueous and organic media, offering a sustainable remediation approach. The bimetallic complexes **Ru4** [(*p*-cymene)$_2$(RuCl)$_2$L^4] and **Ru5** [(*p*-cymene)$_2$(RuCl)$_2$L^5] were derived from the precursor complex [(*p*-cymene)$_2$RuCl$_2$]$_2$ and Schiff base ligands 6′-((1*E*,1′*E*)-((3,3′,5,5′-tetraisopropyl-[1,1′-biphenyl]-4,4′-diyl)bis(azaneylylidene))bis(methaneylylidene)) bis(3,5-dibromophenol) (**H$_2$L^4**) and 2-((*E*)-((4′-(((*E*)-(2-hydroxynaphthalen-1-yl)methylene)amino)-3,3′,5,5′-tetraisopropyl-[1,1′-biphenyl]-4-yl)imino)methyl)naphthalen-1-ol (**H$_2$L^5**), respectively. This Ru(II) bimetallic catalytic system enables complete hydrogenation of azoarenes in water using formic acid/formate buffer as a hydride source. With a catalyst loading of just 0.1 mol% (**Ru1** and **Ru3–Ru5**), azoarenes are efficiently converted to anilines in excellent yields. Furthermore, these catalysts facilitate the dehydrogenative coupling of azoarenes with benzyl alcohols, selectively yielding secondary amines or imines at a low catalyst loading (0.5 mol%). Mechanistic investigations using NMR, ESI-MS, and detailed density functional theory (DFT) calculations provide detailed insights into Ru(II)-mediated azo bond activation. This work broadens the scope of Ru(II)-catalyzed hydrogenation under mild, aqueous conditions and establishes a foundation for sustainable catalytic strategies in environmentally friendly transformations.

1. Introduction

Amines play a pivotal role in organic synthesis across various industries, such as fine chemicals, agrochemicals, and pharmaceuticals.[1,2] Considerable efforts have been focused on the development of efficient methods for large-scale amine production. Common approaches for amine synthesis include dehydrohalogenation reactions,[3] reduction of amides and imines,[4–6] reductive amination (RA) using carbonyls,[7–9] borrowing hydrogenation of alcohols,[10,11] and hydrogenation of nitriles,[12] often catalyzed by transition metal catalysts. Furthermore, hydrogenation of azoarenes presents a viable route for the production of amines and nitrogen-containing compounds due to their intrinsic nitrogen content, making them valuable nitrogen sources. Azoarenes are extensively utilized in the textile and leather industries as dyes.[13,14] However, their use poses environmental challenges, primarily due to the discharge of persistent colored waste and the presence of xenobiotic compounds resistant to biodegradation.[15]

Consequently, there is a pressing need for effective methods to address the environmental concerns associated with azo dye degradation. The hydrogenation of azoarenes (N=N bond) is commonly associated with hydrazine reduction or N_2 reduction and has been a subject of investigation.[16,17] Transfer hydrogenation (TH) of various unsaturated bonds, such as imines, carbonyl, and nitrile bonds, has been well explored.[12,18–20] However, the hydrogenation of recalcitrant N=N bonds of azoarenes has received less attention due to their lower reactivity and bond polarity. Thus, the conversion of azoarenes into primary amines, secondary amines, or imines is a desirable although challenging chemical transformation.[21–25]

Various methods have been explored for the transformation of azoarenes to amines involving heterogeneous and bio-catalyzed reactions.[26] However, many of these methods suffer from drawbacks like high costs, generation of hazardous by-products, excessive sludge production, incomplete purification, and low efficiency.[27] Frediani and coworkers reported the hydrogenation of azobenzene using a ruthenium catalyst under H_2 pressure.[28] Subsequently, Lin and co-workers reported a Co-MOF-catalyzed reduction of hydroazobenzene and azoarenes to aniline under H_2 pressure, although this

Department of Chemistry, Indian Institute of Technology Bombay, Powai, Mumbai 400 076, India. E-mail: rmv@chem.iitb.ac.in, rajaraman@chem.iitb.ac.in

approach was limited to a single substrate.[29] Basallote and co-workers reported another heterogeneous catalytic method for the hydrogenation of azobenzene into aniline employing molybdenum clusters.[22] On the other hand, Milstein co-workers introduced a significant development by showcasing the first homogeneous manganese-catalyzed hydrogenation of azobenzene into anilines.[23] More recently, Kundu and co-workers have developed the heterogeneous Co-SAC catalyzed transfer hydrogenation of azo bonds into anilines using ethanol and methanol as a hydrogen source.[30] Recently, Daw and co-workers reported that a terpyridine ligand-based ruthenium complex efficiently catalyzes the full hydrogenation of azoarenes to aminoarenes at elevated temperatures using isopropanol as a hydride source.[31] However, no example to date demonstrates the selective transfer hydrogenation of azoarenes to anilines in water as the reaction medium, and a detailed mechanistic study of this transformation remains unexplored.

Besides, the use of azoarenes as a nitrogen source for the eco-friendly synthesis of imines and secondary amines mediated by a transition metal catalyst remains an underexplored field. To date, there are only two reports known for dehydrogenative coupling of alcohols with azoarenes to produce imines or amines.[24,25] In a recent development, Kundu and co-workers reported a heterogeneous cobalt catalyst for the degradation of azoarenes to imines using benzyl alcohol.[24] Similarly, Punji and coworkers demonstrated the use of azoarenes for the nickel-catalyzed synthesis of imines and amines using benzyl alcohol *via* a hydrogen borrowing strategy.[25] These studies underscore the growing need for more sustainable and efficient methods to convert azo compounds into valuable amine compounds without relying on high-pressure hydrogen gas.

Bimetallic catalysts have been shown to achieve significant increases in both selectivity and reaction rate in metal-catalyzed reactions compared to their monometallic counterparts. A large number of examples of bimetallic catalysts have been reported in the literature for various organic transformations, such as transfer hydrogenation of ketones,[32] hydrosilylation,[33] propargylic reduction,[34] hydroamination,[35] and cycloisomerisation.[36] We have recently reported novel bimetallic Ru(II) Schiff base complexes for reductive amination in water,[37] one-pot quinoline synthesis,[38] β-alkylation of secondary alcohols,[39] and hydrogenation reactions.[40,41] These studies consistently highlight that bimetallic complexes are more efficient than their monometallic counterparts. Nevertheless, despite these advances, the use of bimetallic catalysts in azoarene hydrogenation and dehydrogenative coupling has remained largely unexplored, and to the best of our knowledge, our study represents the first report in this specific context.

Herein, we report on the hydrogenation and dehydrogenative coupling of azoarenes for the selective synthesis of aniline, secondary amines, and imines using bimetallic Ru(II) catalysts that do not require high-pressure H_2 as a hydride source. This complete study is complemented by DFT calculations for detailed insights into the mechanism of reaction for amines and their derivatives.

2. Results and discussion

2.1 Synthesis and characterization of H_2L^4, H_2L^5, Ru4 and Ru5

Recently, we reported the synthesis of binuclear **Ru1** and **Ru3** complexes, as well as a mononuclear **Ru2** complex, which were employed as catalysts for RA and TH reactions.[37,41] These Ru(II) complexes, specifically **Ru1**, featuring a pseudo-C_2-symmetric N,O-donor ligand, demonstrated high efficiency at low loadings for secondary amine synthesis compared to their mononuclear counterpart, **Ru2**.[37] Thus, the utilization of C_2-symmetric ligands has shown advantages in the development of efficient bimetallic catalyst systems. To further tailor the electronic and steric properties associated with the ligand scaffold, we designed new Schiff base ligands, $\mathbf{H_2L^4}$ and $\mathbf{H_2L^5}$, incorporating distinct substituents for the synthesis of **Ru4** and **Ru5** complexes (Scheme 1). Although they do not bear classic hydrophilic substituents, the resulting complexes exhibit sufficient aqueous dispersibility due to the presence of polar imine and phenolic functionalities, which allow them to operate efficiently in water without precipitation. Additionally, the introduction of tetraisopropyl groups was intended to enhance catalyst stability and maintain the integrity of the Ru-ligand scaffold, while supporting cooperative bimetallic reactivity. We deliberately prioritized these structural and electronic considerations over solubility modification, as the incorporation of strongly hydrophilic groups can sometimes destabilize the coordination environment or diminish productive metal–substrate interactions. Thus, the chosen ligand framework achieves a balanced compromise between water compatibility and the steric/electronic features required for efficient catalysis in aqueous media. $\mathbf{H_2L^4}$ and $\mathbf{H_2L^5}$ were synthesized through the condensation of 2,2′,6,6′-tetraisopropylbenzidine (TIBZ) with 3,5-dibromosalicylaldehyde or 2-hydroxynaphthaldehyde, respectively, and catalyzed by formic acid (Scheme 1).[42,43] The resulting pure products were obtained as yellow crystals through recrystallization of the crude residue in a methanol and dichloromethane solvent mixture (3 : 2 v/v) under ambient conditions.

In the FT-IR spectra of $\mathbf{H_2L^4}$ and $\mathbf{H_2L^5}$, bands observed at around 3428 and 3367 cm^{-1}, respectively, signify the existence of a phenolic –OH group. The C–H stretching vibration of the alkyl groups is observed in the range of 3050–2900 cm^{-1}. The presence of the imine (–N=CH–) linkage is observed in the FT-IR spectra of $\mathbf{H_2L^4}$ and $\mathbf{H_2L^5}$ at 1640 cm^{-1} and 1631 cm^{-1}, respectively (Fig. S1). The ESI-MS study shows an intense molecular ion peak corresponding to $[M + H]^+$ at m/z 876.971 for $\mathbf{H_2L^4}$ and 661.376 for $\mathbf{H_2L^5}$ (Fig. S2 and S3). In the ^{1}H NMR spectra of the Schiff bases, the presence of a singlet in the region of δ ~8.0–9.2 ppm (δ 8.27 ppm for $\mathbf{H_2L^4}$ and $\mathbf{H_2L^5}$ at δ 9.15 ppm) corresponds to the imine (–N=C*H*–) protons. The absence of an amine (–NH_2) proton peak rules out incomplete condensation (Fig. S4 and S6). ^{13}C NMR signals are consistent with the desired product (Fig. S5 and S7).

The bimetallic Ru(II) complexes **Ru4** and **Ru5** were prepared in good yields through the reaction of $\mathbf{H_2L^4}$ and $\mathbf{H_2L^5}$ ligands

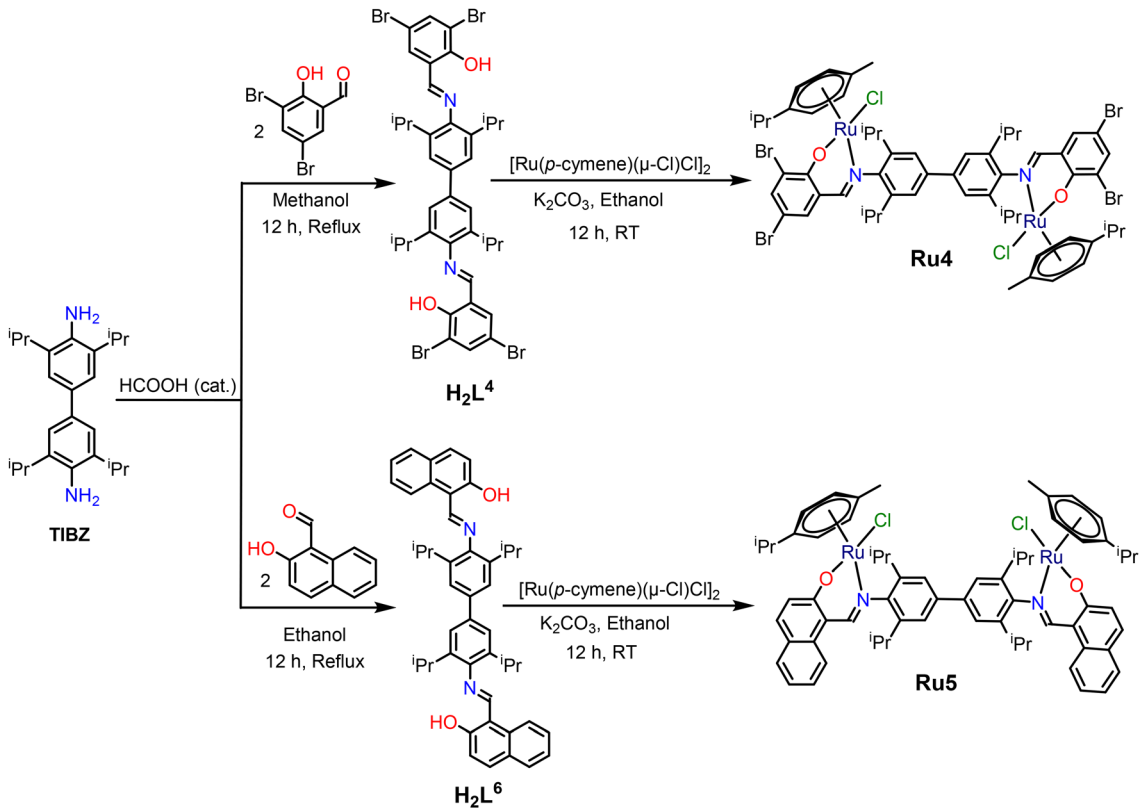

Scheme 1 Synthesis of H_2L^4, H_2L^5, **Ru4** and **Ru5**.

with [Ru(*p*-cymene)(μ-Cl)Cl]$_2$. In a typical synthesis, a Schiff base ligand and potassium carbonate were dissolved in ethanol to obtain potassium salt of the Schiff base. The deprotonated Schiff base undergoes a reaction with [Ru(*p*-cymene)(μ-Cl)Cl]$_2$ at room temperature for 12 h. The resulting crude products precipitate out as dark red solids (Scheme 1), which were purified by recrystallization from an ethanol and dichloromethane mixture to obtain the analytically pure products in the form of dark red crystals.

In the FT-IR spectra of **Ru4** and **Ru5**, the absence of a broad band corresponding to the phenolic –OH group indicates the formation Ru–O linkages. Furthermore, the shifting of the imine stretching band to a lower wavenumber of 1621 cm^{-1} in **Ru4** and 1625 cm^{-1} in the case of **Ru5** (H_2L^4: 1640 and H_2L^5: 1631 cm^{-1}) suggests the formation of the Ru–N=C– linkage in these complexes (Fig. S1).

The ^{1}H NMR spectra obtained for **Ru4** and **Ru5** complexes are consistent with the molecular structure. In the ^{1}H NMR spectra of both complexes, six doublets corresponding to the proton of the methyl groups of isopropyl moieties and three septets for the isopropyl groups of the *p*-cymene and benzidine moieties were observed in the region of δ 1–2 ppm and δ 2–4 ppm, respectively (Fig. S8 and S10). Four doublets were observed in the region between δ 4.30–5.50 ppm for the aromatic protons of the *p*-cymene ring in the ^{1}H NMR spectra of **Ru4** and **Ru5** (Fig. S8 and S10). The ^{13}C NMR spectral (Fig. S9 and S11) signals are consistent with the structure of the desired products. The ESI-MS spectra show an intense molecular ion peak corresponding to $[M + CH_3CN + H]^+$ at *m*/*z* 1457.979 for **Ru4** (Fig. S12) and $[M - Cl]^+$ at *m*/*z* 1165.347 for **Ru5** (Fig. S13), providing additional evidence for the formation of complexes.

The UV-vis absorption spectra of H_2L^4, H_2L^5, **Ru4** and **Ru5** were recorded in dichloromethane at room temperature (Fig. 1). Both H_2L^4 and H_2L^5 ligands exhibit three absorption bands in the range of 220–800 nm (235, 275, and 347 nm for H_2L^4 and 235, 320, and 375 nm for H_2L^5) corresponding to n → σ*, π → π*, and n → π* transitions. The complex **Ru4** displayed a sharp band with the maximum intensity at 265 nm, whereas **Ru5** exhibited three intense absorption bands at 225, 269, and 324 nm corresponding to intra-ligand transitions. The broad absorption band around 457 nm for **Ru4** and 450 nm for **Ru5** in UV-visible spectra were assigned to dπ → π* charge transfer transition, *i.e.* metal-to-ligand charge transfer (Table S1).[37]

H_2L^4 and H_2L^5 were recrystallized under ambient conditions by slow evaporation of the methanol and dichloromethane solvent mixture to yield needle-shaped yellow crystals. In H_2L^4, the imine (–N=CH) bond distance for N(1)–C(7) is 1.257(6) Å (Fig. 2) and in H_2L^5, the distance of the imine (–N=CH) bond for N(1)–C(11) is 1.286(3) Å (Fig. 3). The C(7)–N(1)–C(8) and C(32)–N(2)–C(23) bond angles in H_2L^4 are 116.9(4)° and 120.1(4)°, respectively. In the case of H_2L^5, the C(37)–N(2)–C(27) and C(11)–N(1)–C(12) bond angles are 121.5(1) and 121.9(1)°, respectively. In the molecular structure

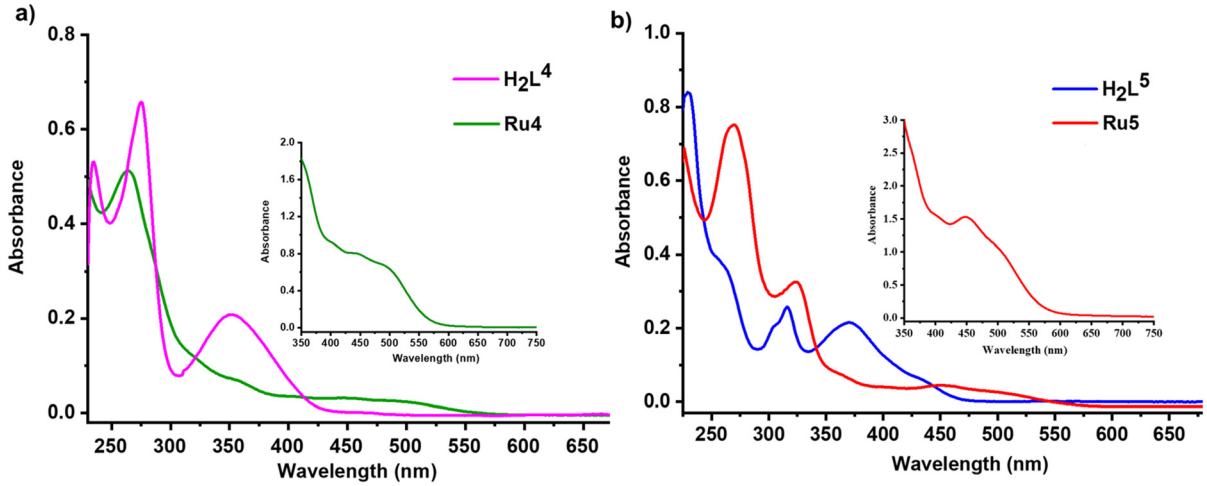

Fig. 1 UV-vis spectra of (a) H_2L^4 and **Ru4** and (b) H_2L^5 and **Ru5** in dichloromethane.

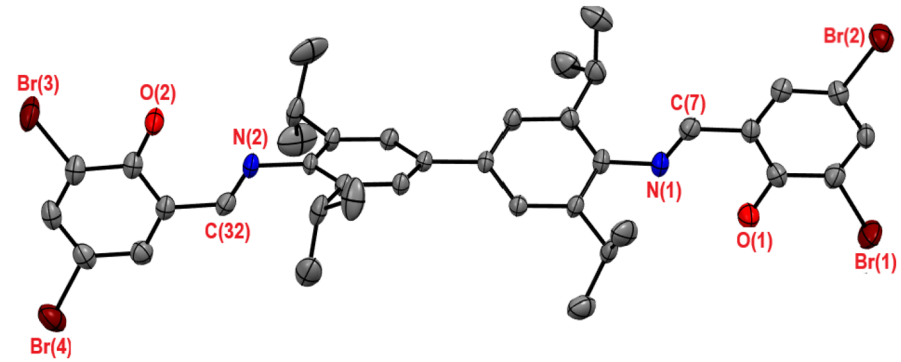

Fig. 2 Molecular structure of H_2L^4 with 50% probability thermal ellipsoid. Hydrogen atoms are omitted for clarity. Selected bond lengths (Å) and bond angles (°): N(1)–C(7), 1.257(6); N(2)–C(32), 1.255(6) Å; C(7)–N(1)–C(8), 116.9(4); C(32)–N(2)–C(23), 120.1(4) C(21)–C(20)–C(11)–C(10), 33.7(5)°. For additional bond lengths and angles, see Table S2.

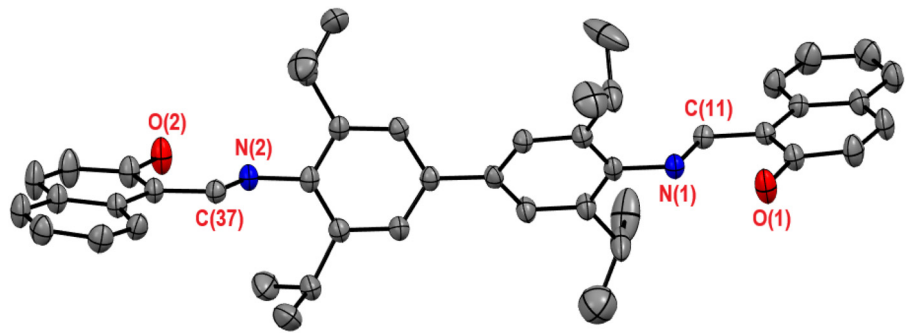

Fig. 3 Molecular structure of H_2L^5 with 50% probability thermal ellipsoid. Hydrogen atoms are omitted for clarity. Selected bond lengths (Å) and bond angles (°): N(1)–C(11), 1.286(3); N(2)–C(37), 1.(3); O(2)–C(39), 1.341(3); O(1)–C(2), 1.341(3) Å; C(37)–N(2)–C(27), 121.5(1); C(11)–N(1)–C(12), 121.9 (1); C(25)–C(24)–C(15)–C(16), 35.8(2)°. For additional bond lengths and angles, see Table S3.

of both Schiff bases, the binding sites are positioned in a *trans* orientation to each other. The two interconnected phenyl rings are twisted by an angle of 35.8(2)° in $\mathbf{H_2L^4}$ and 43.76° in $\mathbf{H_2L^5}$.

Suitable single crystals for X-ray diffraction analysis of **Ru4** and **Ru5** were grown by slow evaporation of the crude product in an ethanol–dichloromethane mixture under ambient conditions. In the molecular structure of both complexes, the ruthenium centers adopt an approximate piano stool-type coordination geometry. Each ruthenium atom is coordinated to the nitrogen atom of the imine, an oxygen atom of the

phenolate group of the Schiff base, a chloride ion, and a *p*-cymene moiety (in η^6-fashion). The imine (–N=CH) bond distances in the complexes are longer compared to the parent Schiff base ligands. In the case of **Ru4**, the N(1)–C(7) distance is 1.292(5) Å (Fig. 4), and the N(1)–C(11) distance in **Ru5** is 1.290(6) Å (Fig. 5). The bond angles between the ruthenium, oxygen, nitrogen, and chlorine atoms for **Ru4** are O(1)–Ru(1)–Cl(1) = 85.38(8)° and O(2)–Ru(2)–Cl(2) = 84.79(8)°, and in the case of **Ru5**, the bond angles are O(1)–Ru(1)–Cl(1) = 83.69(9)° and O(2)–Ru(2)–Cl(2) = 83.87(9)° (Fig. 4 and 5). The Schiff base binding sites are observed on opposite sides in the molecular structure of the ligands. However, during the formation of the complexes, there is a change in the arrangement around the connected phenyl groups, resulting in the Schiff base binding sites of the ligands being positioned on the same side in the molecular structure of both complexes. The non-planarity observed in both the ligands and their complexes is attributed to the presence of bulky isopropyl groups. The presence of these groups induces a deviation from coplanarity in the two phenyl rings, resulting in a twist angle (torsional angle) of 43.76° in **Ru4**, which is higher than that of $\mathbf{H_2L^4}$. On the other hand, in the case of **Ru5**, the twist angle is 12.2 (5)°, which is

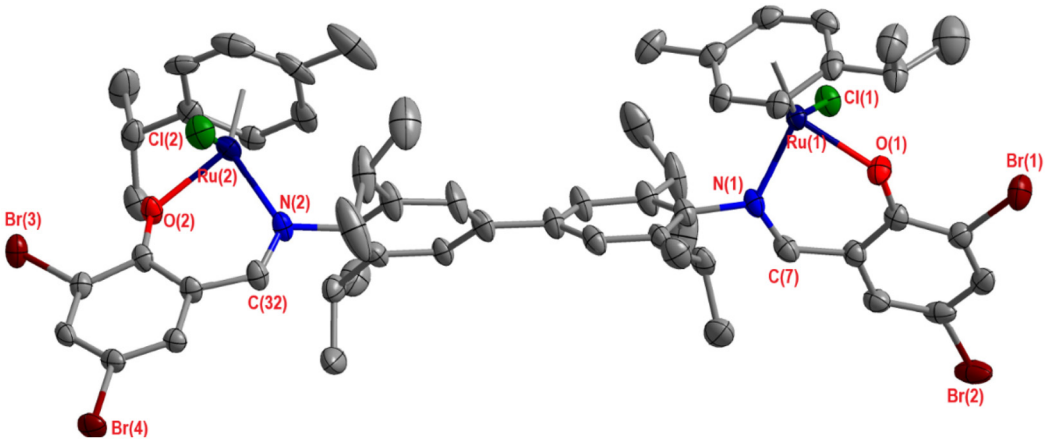

Fig. 4 Molecular structure of **Ru4** with 50% probability thermal ellipsoid. Solvent molecules and hydrogen atoms are omitted for clarity. Selected bond lengths (Å) and bond angles (°): Ru(1)–Cl(1), 2.425(1); Ru(1)–O(1), 2.059(3); Ru(1)–N(1), 2.120(3); Ru(2)–Cl(2), 2.437(1); Ru(2)–O(2), 2.059(3); Ru(2)–N(2), 2.114(3); N(1)–C(7), 1.292(5); N(2)–C(32), 1.3(5) Å; O(1)–Ru(1)–Cl(1), 85.38(8); O(1)–Ru(1)–N(1), 85.6(1); O(2)–Ru(2)–Cl(2), 84.79(8); O(2)–Ru(2)–N(2), 86.6(1); N(2)–Ru(2)–Cl(2), 84.5(9); C(12)–C(11)–C(20)–C(21), 43.9(4)°. Centroid of *p*-cymene to Ru distance for Ru(1) 1.678(4) Å and Ru(2) 1.676(4) Å in the **Ru4** complex. For additional bond lengths and angles, see Table S4.

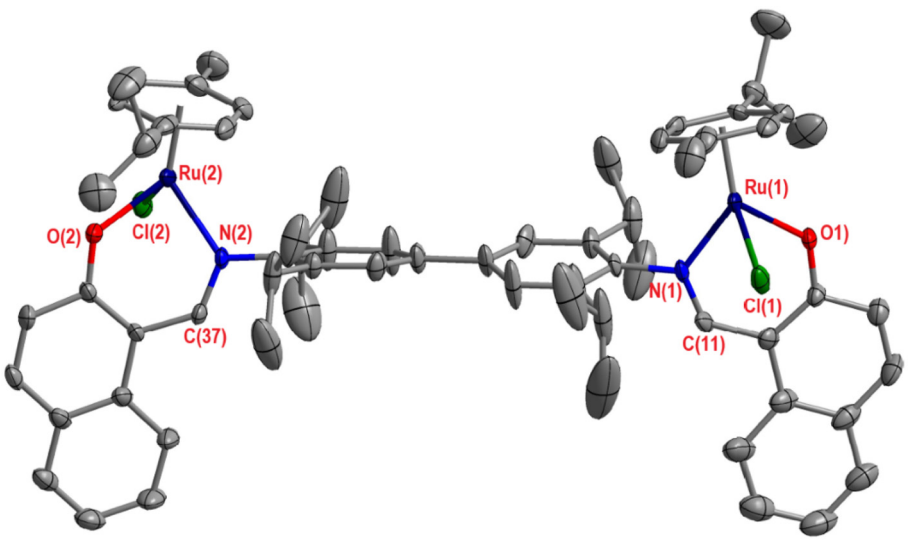

Fig. 5 Molecular structure of **Ru5** with 50% probability thermal ellipsoid. Solvent molecules and hydrogen atoms are omitted for clarity. Selected bond lengths (Å) and bond angles (°): Ru(1)–Cl(1), 2.433(1); Ru(1)–O(1), 2.053(3); Ru(1)–N(1), 2.101(4); Ru(2)–Cl(2), 2.434(1); Ru(2)–O(2), 2.05(3); Ru(2)–N(2), 2.093(3); N(1)–C(11), 1.290(6); N(2)–C(37), 1.294(5) Å; O(1)–Ru(1)–Cl(1), 83.69(9); O(1)–Ru(1)–N(1), 85.9(1); N(1)–Ru(1)–Cl(1), 86.3(1); O(2)–Ru(2)–Cl(2), 83.87(9); O(2)–Ru(2)–N(2), 86.1(1); N(2)–Ru(2)–Cl(2), 86.32(1); C(15)–C(16)–C(19)–C(24), 12.2(5)°. Centroid of *p*-cymene to Ru distance for Ru(1) and Ru(2) is 1.670(5) Å in the **Ru5** complex. For additional bond lengths and angles, see Table S5.

smaller compared to that found in H_2L^5. This non-coplanar arrangement contributes to the overall non-planar nature of the molecules, giving rise to a C_2-symmetric configuration.

3. Transfer hydrogenation of azoarenes to aniline in aqueous medium

To explore the catalytic activity of Ru(II) complexes (**Ru1–Ru5**) (Fig. 6) in the transfer hydrogenation of azoarenes to aniline, the reaction conditions were first optimized by using azobenzene as the model substrate and **Ru1** as a catalyst (Fig. 6).

The model reaction was carried out in water. Formic acid/formate buffer has been chosen due to its mild nature resulting in greater selectivity for the desired products. In our earlier work,[37,41] we observed that the pH of the buffer played a crucial role in the transfer hydrogenation reaction. Thus, we varied the pH value of the formate buffer in the range of 4.5 to 3.0. When the reaction was carried out with the **Ru1** catalyst (0.1 mol%) in the presence of formic acid/formate buffer (pH 4.5) as a hydride source at 80 °C in water for 8 h, only 41% yield of aniline was obtained (Table 1, entry 1). To improve the yield of the product, the reaction conditions were varied. The best result was obtained for the run carried out by using 0.1 mol% of **Ru1** and formic acid/formate buffer at pH 3.5 and for 5 h in water at 80 °C (Table 1, entry 3).

The selection of pH 3.5 for hydrogenation is supported by both experimental optimization and mechanistic considerations. Our previous reports on homobimetallic Ru(II) complexes[37,41] have shown that the stability and reactivity of the key catalytic intermediates, Ru-hydride and Ru-formate, are strongly pH-dependent. At low pH, Ru-hydride species are readily protonated or diverted into unproductive pathways, while at high pH, the decomposition of $HCOO^-$ to CO_2 and HCO_3^- suppresses the formation of Ru-formate. In contrast, at pH 3.5 both Ru-hydride and Ru-formate are generated and stabilized in optimal concentrations, creating the most favorable conditions for efficient hydride transfer. When the reaction was carried out at various temperatures between 30 °C and 80 °C, the maximum yield was obtained at 80 °C, showing that the present approach is more energy efficient as compared to earlier reported methods.[23,24] The reaction does not proceed in the absence of a catalyst or buffer, highlighting the key roles of both in the reaction (Table 1, entries 10 and 11). To check the effect of organic solvents on improving the yields/reaction period, the reaction was performed in protic organic solvents such as isopropanol and ethanol in the presence of bases, resulting in poor yields of aniline (Table 1, entries 12–14).

Regarding the stability of the catalyst and the imine bonds in the Schiff-base ligands of the Ru(II) complexes, these remain stable under the water/formic acid–formate buffer conditions. This stability arises primarily from two factors: (i) the steric protection provided by the bulky 2,6-diisopropylphenyl substituents around the imine moiety, which hinder nucleophilic attack by water, and (ii) coordination of the imine nitrogen to the Ru center, which strengthens the C=N bond and significantly reduces its susceptibility to hydrolysis. In addition, the reactions are conducted at moderate temperatures and at a buffered pH of ~3.5, conditions that suppress acid-catalyzed hydrolysis.

The stability of **Ru1** has previously been tested under both reaction conditions and in water.[37] These studies confirmed that the catalyst remains stable, and **Ru1** could be successfully reused over multiple cycles, as we have previously demonstrated for the transfer hydrogenation of aldehydes.[41] In the current hydrogenation of azobenzenes, however, we were unable to recover the Ru-catalysts effectively. The reaction

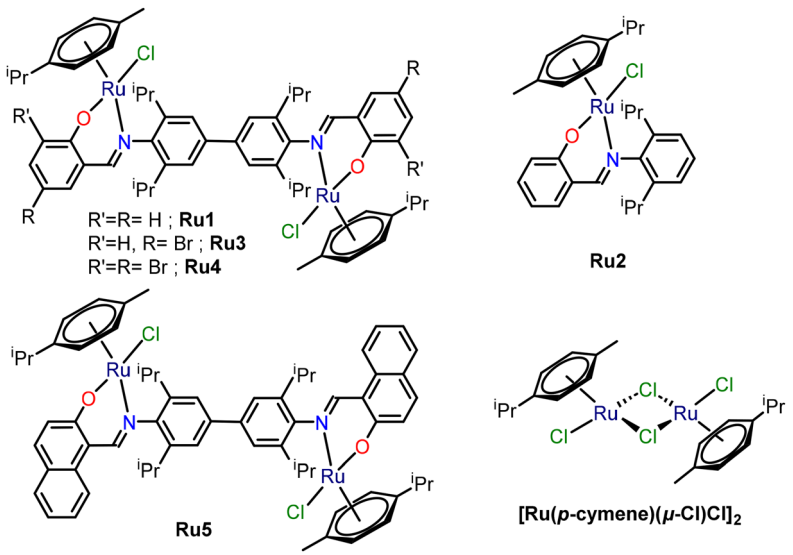

Fig. 6 Bimetallic and monometallic catalysts were employed in the present study.

Table 1 List of reaction conditions for transfer hydrogenation of azobenzene

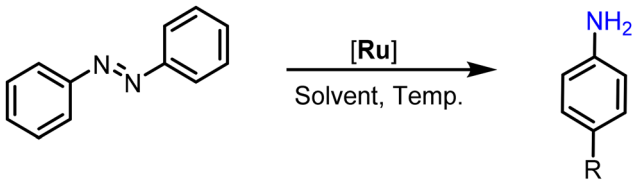

Entry	Cat. (mol%)	Solvent	Temp. (°C)	Base	pH	Time (h)	Yield[f] (%)	Con.[f] (%)
1	0.1	H_2O	80	HCOONa : HCOOH	4.5	8	41	50
2	0.1	H_2O	80	HCOONa : HCOOH	4.0	8	49	53
3	**0.1**	**H_2O**	**80**	**HCOONa : HCOOH**	**3.5**	**5**	**93**	**100**
4	0.01	H_2O	80	HCOONa : HCOOH	3.5	5	87	93
5	0.5	H_2O	80	HCOONa : HCOOH	3.5	5	95	100
6	0.1	H_2O	60	HCOONa : HCOOH	3.5	5	83	88
7	0.1	H_2O	40	HCOONa : HCOOH	3.5	5	57	62
8	0.1	H_2O	RT	HCOONa : HCOOH	3.5	5	24	33
9	0.1	H_2O	80	HCOONa : HCOOH	3.0	5	29	12
10	0	H_2O	80	HCOONa : HCOOH	3.5	5	0	0
11	0.1	H_2O	80	—	3.5	5	0	0
12	0.1	^{i}PrOH	90	KOH	—	6	57	61
13	0.1	^{i}PrOH	90	KO^{t}Bu	—	6	69	78
14	0.1	EtOH	90	KO^{t}Bu	—	6	40	52
15[a]	0.2	H_2O	80	HCOONa : HCOOH	3.5	5	37	48
16[b]	0.1	H_2O	80	HCOONa : HCOOH	3.5	5	91	97
17[c]	0.1	H_2O	80	HCOONa : HCOOH	3.5	5	90	98
18[d]	0.1	H_2O	80	HCOONa : HCOOH	3.5	5	95	100
19[e]	0.1	H_2O	80	HCOONa : HCOOH	3.5	5	15	19

Reaction conditions: azobenzene (0.5 mmol), 2 mL of solvent, reaction bath temperature 90–30 °C, time 4–8 h. [a] Use of **Ru2**. [b] Use of **Ru3**. [c] Use of **Ru4**. [d] Use of **Ru5**. [e] Use of $[Ru(p\text{-cymene})Cl_2]_2$. [f] Yields and conversions are calculated using GC-MS.

mixture formed a sticky residue, which hindered clean separation and prevented catalyst reuse.

After optimization, a comprehensive study of the applicability of the current approach to various azo substrates using **Ru1** as a catalyst was carried out (Scheme 2). Initially, symmetrical azobenzene derivatives were used as starting materials under optimized reaction conditions for the synthesis of anilines. The reactions of a variety of mono-substituted and di-substituted azo compounds (**1a–17a**) afforded good yields of the desired anilines (**1b–17b**). The electron-donating substituents on azoarene rings such as –^{i}Pr (**2a**), –^{t}Bu (**3a**), –Me (**4a**), and –OMe (**5a**) resulted in a high yield of anilines **2b** (95%), **3b** (98%), **4b** (94%) and **5b** (97%), respectively. In contrast, the presence of electron-withdrawing substituents at the *para* positions of the aromatic ring of the azobenzene derivatives (**6a**, **7a** and **8a**) resulted in lower yields of the corresponding **6b** (71%), **7b** (79%) and **8b** (86%) anilines. Following this, the reaction was repeated with various di- and trisubstituted azo compounds (**9a–11a**), leading to the formation of the corresponding anilines **9b–11b** in moderate yields. However, an *ortho*-substituted azoarene (**9a**) displayed relatively lower reactivity, likely due to steric hindrance. Azo compounds containing a heterocycle (**12a**) efficiently transformed into the corresponding aniline **12b** in 87% yield. Next, we subjected various azo compounds containing reducible functional groups (**13a–16a**), resulting in the desired anilines **13b** (79%), **14b** (73%) and **15b** (66%) in moderate to high yields. It is important to note that functional groups such as –CO_2H (carboxylic acid), –COMe (ketone) and –CO_2Me (ester) groups remained unaltered under reaction conditions, which underscores the high chemoselectivity of the bimetallic **Ru1** catalyzed approach for the transfer hydrogenation of azo bonds (Scheme 2).

This reaction was further probed with unsymmetrical azo derivatives. As shown in Scheme 3, unsymmetrical azo derivatives bearing two different aromatic groups in the presence of **Ru1** undergo complete hydrogenation to produce the corresponding anilines in high yields. The electron-donating substituents at the *para*-position of the aryl ring such as –^{i}Pr (**1c**), –^{t}Bu (**2c**), –Me (**3c**), and –OMe (**4c**) afforded the corresponding anilines **1d**, **2d**, **3d**, and **4d** in good yields (Scheme 3). The electron-withdrawing substituted substrates, such as –Cl (**5c**) and –Br (**6c**), also undergo transfer hydrogenation reaction resulting in the formation of the corresponding **5d** and **6d** anilines in moderate to good yields (**5d**: 76% and **6d**: 82%). Even in this case, the functional groups such as acids (**10c**), ketones (**11c**), and nitriles (**12c**) remain unaffected, underscoring chemoselectivity only for the azo bonds (N=N). It is important to highlight that, unlike previously reported catalytic systems where the ketone functionality was hydrogenated, the present method demonstrates greater selectivity towards azo groups.[30,31]

The lower yields observed with electron-deficient azoarenes bearing substituents such as –CO_2H, –COMe, and –CN can be

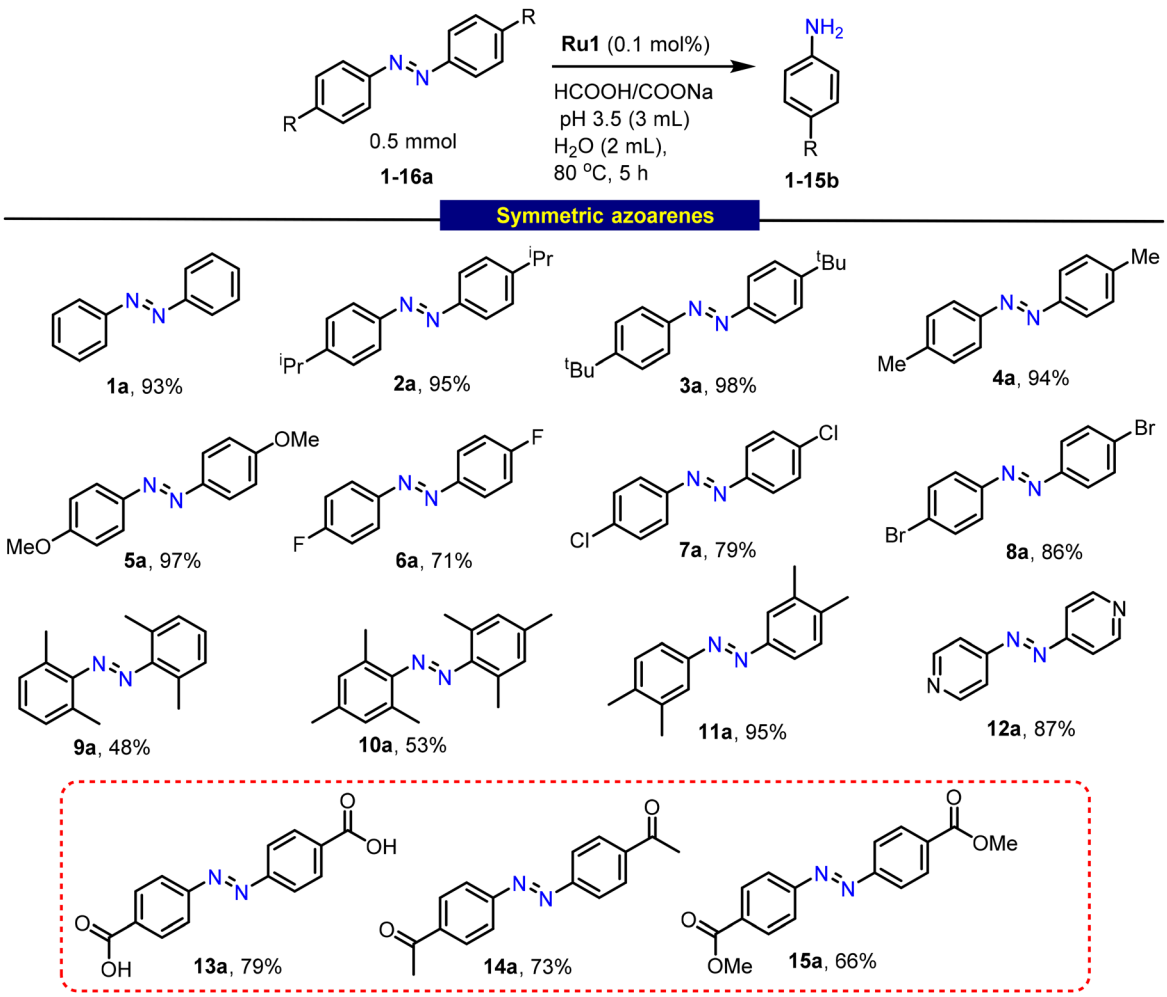

Scheme 2 Substrate scope for the TH of symmetric azoarenes.

primarily attributed to electronic effects rather than steric hindrance. These electron-withdrawing groups decrease the electron density on the azo nitrogen atoms, thereby reducing their coordination ability to the Ru center and slowing the formation of the Ru-azo intermediate that initiates catalysis. Moreover, the resulting anilines formed from these substrates are less nucleophilic, which further hampers downstream imine or amine formation. While steric congestion at the *ortho* positions can exacerbate this effect, in the case of *para*-substituted $-CO_2H$, –COMe, and –CN derivatives, the electronic deactivation dominates, accounting for their relatively sluggish reactivity and reduced yields in our Ru(II) bimetallic system. We initially tested a *p*-nitro substrate, but it was unreactive under the standard conditions, indicating slower dehydrogenation. Additionally, alkyl azo compounds were inefficient under these conditions. For commercially available azo dyes, the reaction with methyl yellow gave the corresponding aniline in 27% yield. In conclusion, the bimetallic **Ru1**-catalyzed transfer hydrogenation method demonstrates a broad substrate scope and tolerance for various functional groups in aqueous medium. Thus, it provides a mild and environmentally friendly approach for the degradation of azo compounds to aniline with high yields.

3.1 Comparative study of bimetallic (Ru1 and Ru3–Ru5) catalysts with a monometallic (Ru2) catalyst

Comparison of the catalysis outcome and computational insights of ruthenium catalysts for reductive amination reaction has revealed the superiority of the bimetallic catalysts over their monometallic counterparts.[37] In this study, we elucidate the reactivity patterns of bimetallic **Ru1**/**Ru3–Ru5** complexes compared to that of monometallic **Ru2** in the context of the TH reaction of azobenzene to aniline. Utilizing selected substrates, including symmetrical electron-donating, electron-withdrawing, and unsymmetrical azobenzenes, we conducted reactions to assess the cooperativity in **Ru1** and **Ru3–Ru5** catalysts (0.1 mol%). Significantly, **Ru1** and **Ru3–Ru5** catalysts displayed similar and effective reactivity patterns with these substrates (Table 2). Conversely, when employing 0.2 mol% of the monometallic **Ru2** complex on the same substrates, the catalytic outcomes differed appreciably from those observed with the bimetallic catalysts (Table 2). This disparity in catalytic

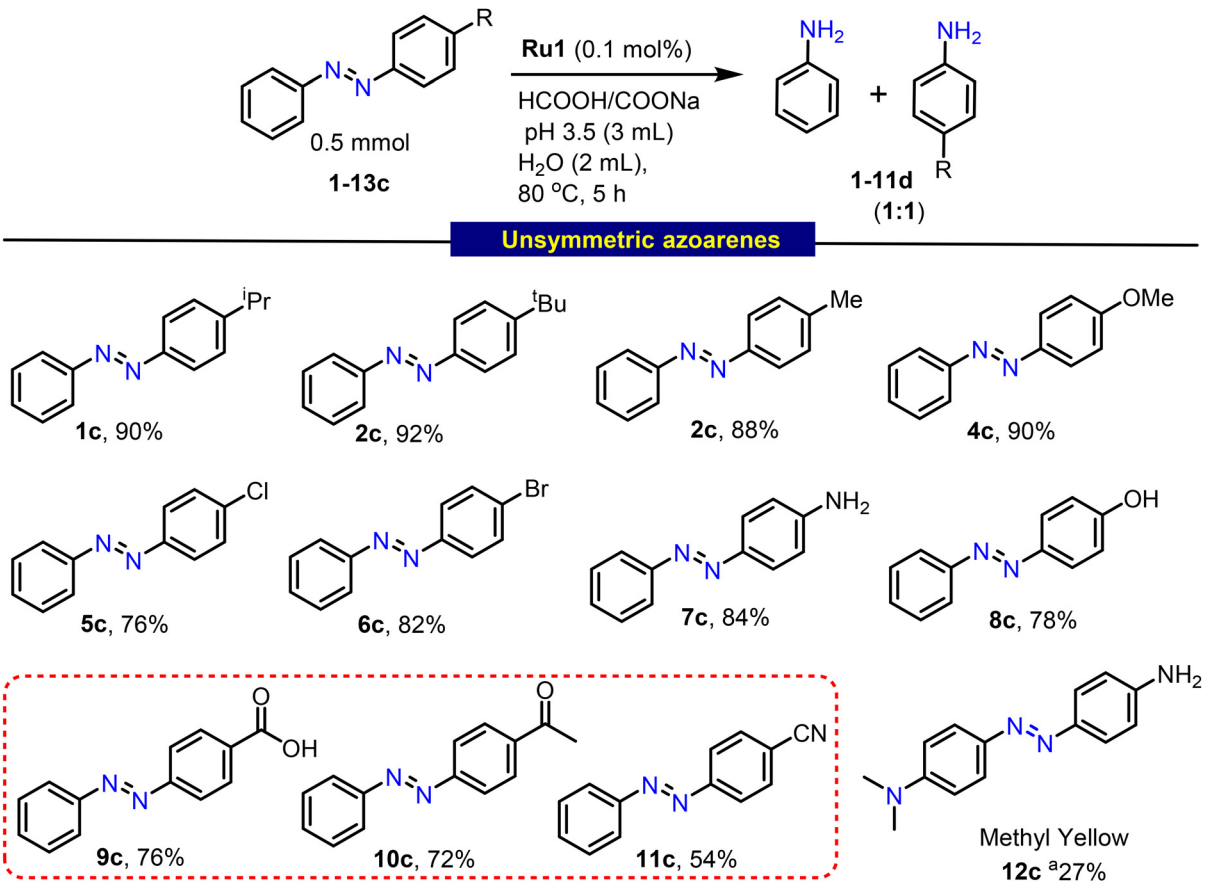

Scheme 3 Substrate scope for the TH of unsymmetric azoarenes, [a]yield by GC-MS.

activity between the bimetallic (**Ru1** and **Ru3–Ru5**) catalysts and the monometallic (**Ru2**) catalyst underscores the superior performance of the bimetallic catalysts in generating active precatalysts (intermediates II and III) within the catalytic cycle.[37] We have compared catalysts at an equal number of active Ru centers. Each molecule of the C_2-symmetric bimetallic complex contains two Ru sites, whereas **Ru2** is mononuclear. Thus, 0.1 mol% bimetallic catalyst (≈0.2 mol% Ru) was matched with 0.2 mol% **Ru2** to equalize total Ru centers and avoid bias from different site counts. This way, the comparison allows us to evaluate whether the two Ru centers within a single bimetallic scaffold act cooperatively and enhance reactivity/selectivity, rather than the performance difference being due to a simple doubling of the active metal. We have also evaluated at equimolar complex loading (0.1 mol% **Ru2**). Under optimized conditions, 0.1 mol% **Ru2** gave lower yields with incomplete conversion of the starting material (Fig. S107).

Under optimized conditions, the reaction of phenylhydrazine resulted in the reductive cleavage of the N–N bond, yielding aniline as the product. This demonstrates that the reaction proceeds *via* reductive cleavage of the N–N bond (Scheme 4).

After conducting optimization, substrate scope, and comparative studies, we carried out investigations to identify the catalytically active species and reaction intermediates using computational methods along with spectroscopic techniques. In **Ru1**, the geometry around Ru(II) is distorted octahedral having the electronic configuration $(d_{xy})^2$ $(d_{xz})^2$ $(d_{yz})^2$ $(d_{x^2-y^2})^0$ $(d_{z2})^0$ with a t_{2g}–e_g gap of 4.23 eV suggesting a strong ligand field and a low-spin ground state.[32,36] The schematic mechanism shown in Fig. 7 based on experimental results has been adapted for our calculations (Fig. 7). In the first step, **Ru1** (species $\mathbf{I_a}$) undergoes chloride ion exchange with the formate ion, resulting in the formation of Ru-formate (species $\mathbf{II_a}$) and this is found to be exothermic by 231.3 kJ mol^{-1}. The facile formation of species $\mathbf{II_a}$ predicted from the calculation is consistent with the experimental observation of the same using mass spectrometry, exhibiting an $[M + H]^+$ ion peak at m/z 1121.300 (Fig. S14). Subsequently, after 20 minutes, species $\mathbf{II_a}$ undergoes β-hydride transfer through CO_2 elimination, resulting in ruthenium–hydride species $\mathbf{III_a}$, the formation of which is found to be 16.8 kJ mol^{-1} exothermic from species $\mathbf{II_a}$, also suggesting favorable formation. This step is favoured by the proximity of the H atom of formate to Ru (H···Ru at species **II** is 2.845 Å) to enable the formation of the Ru–H species. The mass spectrometry analysis also detected the formation of ruthenium–hydride species (Ru-hydride, $\mathbf{III_a}$) $[M - H]^+$ ion at m/z 1031.339 (Fig. S15), offering confidence in the mechanism adapted and the energetics computed. In the next step, the N=N (azo bond) in azobenzene is expected to coordinate with

Table 2 Comparison of **Ru1**/**Ru3**–**Ru5** with **Ru2** for TH of azo compounds

		Aniline derivative yield (%)				
Entry	Substrate	**Ru1** (0.1 mol%)	**Ru2** (0.2 mol%)	**Ru3** (0.1 mol%)	**Ru4** (0.1 mol%)	**Ru5** (0.1 mol%)
1	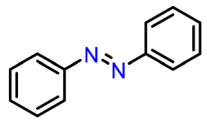	93	37 (21%)[a]	91	90	95
2	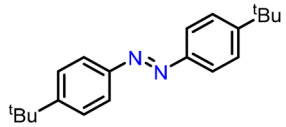	98	48	96	95	98
3	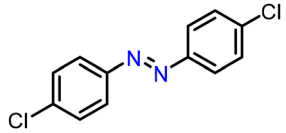	79	28	73	75	81
4	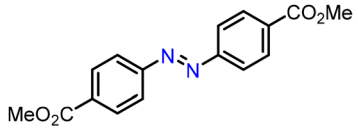	73	21	70	71	69
5	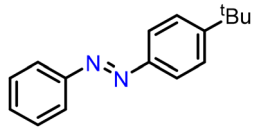	92	34	90	89	93

Reaction conditions: azoarene (0.5 mmol), HCOONa : HCOOH (3 mL, pH 3.5), water (2 mL), 80 °C for 5 h. [a] Use of 0.1 mol% of **Ru2**.

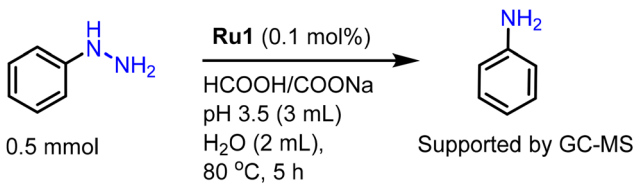

Scheme 4 Hydrogenation of phenylhydrazine using **Ru1**.

the ruthenium center, leading to the formation of species $\mathbf{IV_a}$. For this coordination to take place, the nitrogen atom in the Schiff-base ligand dissociates, generating an unstable 16e$^-$ species, which subsequently binds to the N=N group of azobenzene in an η^2 mode, forming a stable 18e$^-$ complex. As this involves cleavage of the Ru η^2 (Ph–N=N–Ph) bond, this step is found to be endothermic from species $\mathbf{III_a}$ by 199.9 kJ mol^{-1}. However, from the reactant energy, the overall formation is exothermic by 48.2 kJ mol^{-1}. This clearly suggests that the energetic gain obtained in the formation of species III is dissipated during the transition to species $\mathbf{IV_a}$. In the next step, hydride migration to the nitrogen atom of the azo group is expected, leading to the formation of species $\mathbf{V_a}$, and this is facilitated at species $\mathbf{IV_a}$ with the short H···N (azo group) distance of 2.350 Å. The formation of species $\mathbf{V_a}$ is exothermic by 131.8 kJ mol^{-1} from species $\mathbf{IV_a}$ as shown in Fig. 8. In the next step, the second nitrogen atom of the azo group will get protonated from the acid buffer that is added in the reaction leading to the release of phenyl hydrazine and regeneration of species $\mathbf{II_a}$ whose formation is also exothermic, suggesting a facile reaction.

In the subsequent steps, phenyl hydrazine binds to species $\mathbf{III_a}$ (ruthenium–hydride species) through its nitrogen atom, facilitating the formation of species $\mathbf{IV_a}'$, which is accompanied by Ru–N bond cleavage of the Schiff-base ligand. Again, this step is found to be endothermic as this involved cleavage of the Ru–N bond of a 16e$^-$ species. In the next step, a hydride is transferred to the distal nitrogen of hydrazine, leading to the formation of species $\mathbf{V_a}'$. This step breaks the N–N bond of hydrazine and produces one molecule of aniline. An acidic buffer then donates a proton to the remaining nitrogen, forming another aniline molecule. This process regenerates the active catalyst (species $\mathbf{II_a}$) and completes the reaction. The proposed mechanism suggests that the N=N (azo bond) is subsequently hydrogenated through hydrogen transfer to generate intermediate $\mathbf{V_a}$ (Fig. S16). The Ru-azo species is highly reactive and transient under the catalytic conditions, which makes its signal relatively low and prevents reliable quantitative analysis, thus limiting the ability to extract kinetic data.

The same catalytic pathway has been observed for the hydrogenation of azoarenes using the **Ru3–Ru5** complex in the presence of formic acid/formate buffer. The detection of intermediate species, Ru-formate and Ru-hydride, has been successfully accomplished through ESI-MS studies. In the case of **Ru4**, Ru-formate displays a molecular ion peak corresponding to $[M - OCOH]^+$ at m/z 1390.991, and Ru-hydride shows $[M]^+$ at m/z 1348.967 (Fig. S17 and S18).

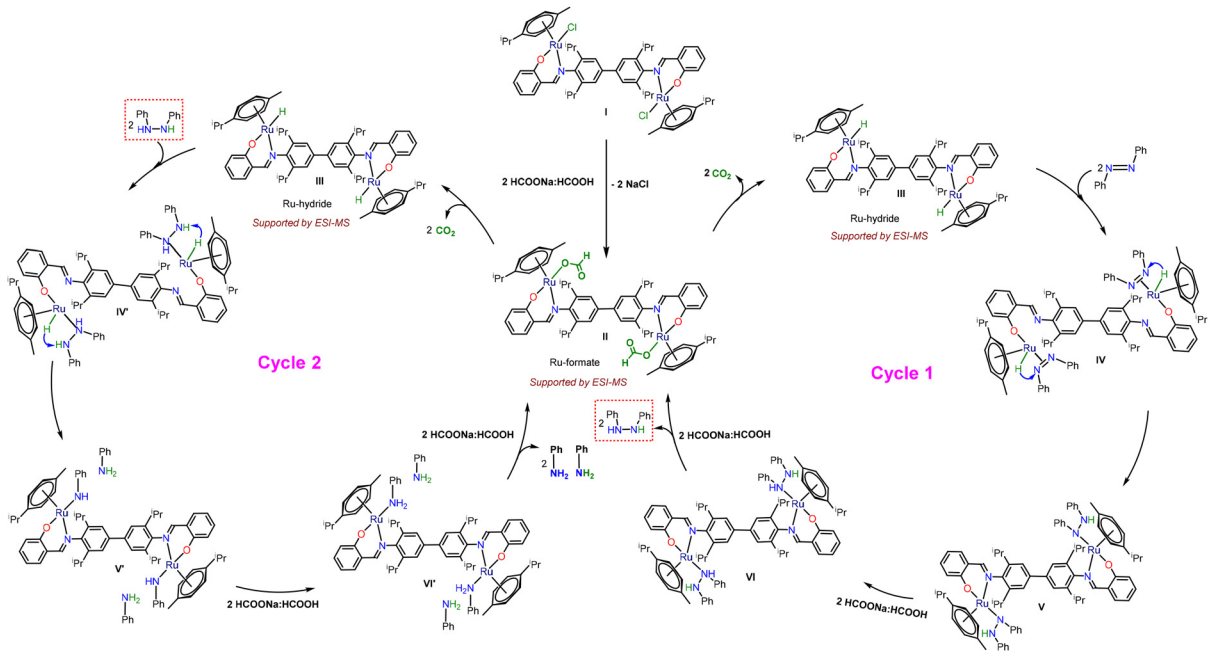

Fig. 7 Probable mechanism of hydrogenation of azobenzene using the **Ru1** catalyst.

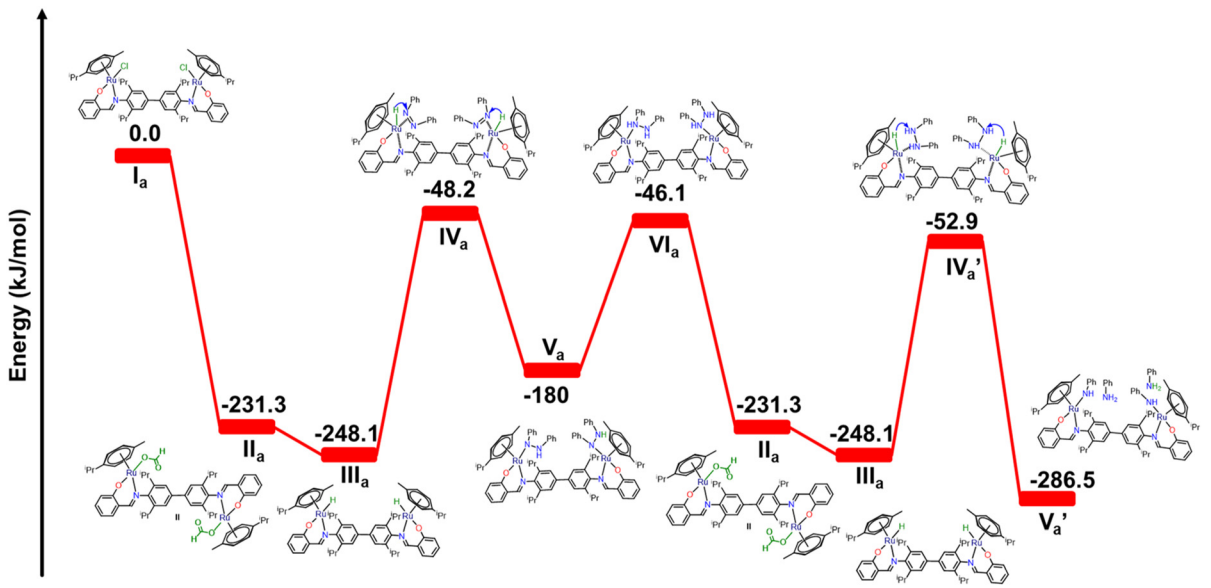

Fig. 8 The computed potential energy profile diagram in solvent phase free energies (Δ*G*), at the B3LYP-D3/def2-TZVP level of theory for reaction pathways of the bimetallic complex.

4. Dehydrogenative coupling of azoarenes with benzyl alcohol

After performing the transfer hydrogenation of azoarenes to anilines, the investigation proceeded to explore the dehydrogenative coupling of azoarenes for the selective synthesis of secondary amines or imines using benzyl alcohol. In the optimization of reaction conditions for achieving selective secondary amine or imine products, azobenzene (**1a**) and benzyl alcohol (**2a**) were chosen as model substrates. We have investigated the dehydrogenative coupling of the azo compound and benzyl alcohol through the activation of the N=N of azobenzene using bimetallic **Ru1** (or **Ru3**–**Ru5**) catalysts (Table 3). Since *N*-alkylation using benzyl alcohol is typically favored at higher temperatures and with increased base loadings, the optimization experiments commenced at a temperature of 110 °C in the presence of a base.[44,45]

Table 3 Optimization of reaction conditions for coupling of benzyl alcohol with azobenzene

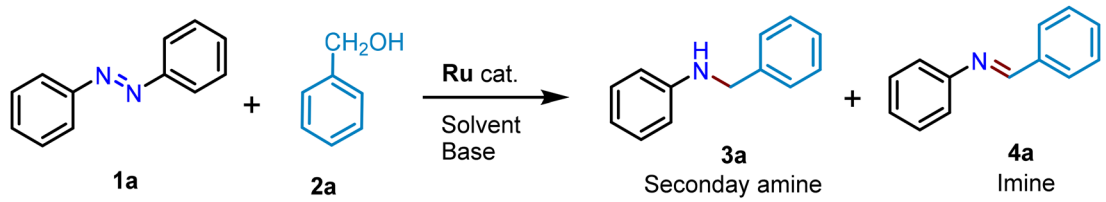

Entry	Cat. (mol%)	Solvent	Base	Time (h)	Temp. °C	Secondary amine (**3a**)[f] (%)	Imine (**4a**)[f] (%)
1	0.3	Toluene	K_2CO_3	12	110	0	52
2	0.3	Toluene	Na_2CO_3	12	110	0	17
3	0.3	Toluene	Cs_2CO_3	12	110	21	60
4	0.3	Toluene	KOH	12	110	20	79
5	0.3	Toluene	KO^{t}Bu	10	110	81	14
6	0.3	Toluene	KOH	10	100	10	72
7	**0.5**	**Toluene**	**KO^{t}Bu**	**6**	**100**	**95**	**4**
8	0.5	Toluene	KOH	6	100	15	84
9	—	Toluene	KO^{t}Bu	6	100	0	0
10	0.5	Toluene	—	6	100	0	0
11	0.5	Dioxane	KO^{t}Bu	6	110	0	29
12	0.5	THF	KO^{t}Bu	6	110	0	26
13	**0.5**	**Toluene**	**NaOH**	**6**	**100**	**0**	**94**
14	0.05	Toluene	NaOH	6	100	0	73
15	0.01	Toluene	NaOH	6	100	0	51
16	0.001	Toluene	NaOH	6	100	0	39
17	0.01	Toluene	KO^{t}Bu	6	110	69	23
18	0.001	Toluene	KO^{t}Bu	6	110	58	41
19[a]	1	Toluene	NaOH	6	100	0	57
20[b]	0.5	Toluene	NaOH	6	100	0	0
21[c]	0.5	Toluene	NaOH	6	100	0	89
22[d]	0.5	Toluene	NaOH	6	100	0	86
23[e]	0.5	Toluene	NaOH	6	100	0	94
24[c]	0.5	Toluene	KO^{t}Bu	6	100	86	12
25[d]	0.5	Toluene	KO^{t}Bu	6	100	91	8
26[e]	0.5	Toluene	KO^{t}Bu	6	100	96	0
27	0.5	Toluene	KO^{t}Bu (0.5 mmol)	6	100	51	10
28	0.5	Toluene	KO^{t}Bu (0.25 mmol)	6	100	37	6

Reaction conditions: azobenzene (0.5 mmol), benzyl alcohol (1.5 mmol or 1.1 mmol), base (1 mmol), 2 mL of solvent, reaction bath temperature 110–50 °C, time 6–12 h. [a] Use of **Ru2**. [b] Use of [Ru(*p*-cymene)Cl_2]$_2$. [c] Use of **Ru3**. [d] Use of **Ru4**. [e] Use of **Ru5**. [f] Isolated yields and conversions are calculated using GC-MS.

The azobenzene (**1a**) is treated with benzyl alcohol (1.5 mmol) (**2a**) with **Ru1** as a catalyst in the presence of K_2CO_3 (1 mmol), delivering 52% of imine (**4a**) (Table 3, entry 1). The choice of base plays a crucial role in the dehydrogenative coupling of azobenzene with benzyl alcohol, as it influences both the formation of the Ru-hydride species and the subsequent *N*-alkylation step. As shown in Table 3, weaker carbonates such as K_2CO_3 and Na_2CO_3 afforded poor yields of both secondary amine (**3a**) and imine (**4a**) due to insufficient deprotonation of benzyl alcohol and slower generation of the active Ru-alkoxide or Ru-hydride intermediate. As shown in Table 3, weaker carbonates such as K_2CO_3 and Na_2CO_3 afforded poor yields of both secondary amine (**3a**) and imine (**4a**) due to insufficient deprotonation of benzyl alcohol and slower generation of the active Ru-alkoxide or Ru-hydride intermediate. Stronger bases such as KOH and NaOH enhanced the formation of the active catalyst species, leading to higher conversion and selectivity; for example, NaOH with **Ru1** selectively produced imine **4a** in 94% yield (entry 13). KO^{t}Bu, a sterically hindered strong base, favored *N*-alkylation over imine formation, resulting in high selectivity toward the secondary amine **3a** (entry 5). These results indicate that both the strength and steric nature of the base modulate the reaction pathway: strong, non-nucleophilic bases promote efficient Ru-hydride formation and control the selectivity between imine and secondary amine products, whereas weaker or less basic salts are insufficient for complete dehydrogenation and coupling under the given conditions. The use of KO^{t}Bu (1 mmol) led to a decrease in the selectivity of **4a** and provided selectively secondary amine **3a** in 81% yield (Table 3, entry 5). Interestingly, when the catalyst loading **Ru1** was increased from 0.1 mol% to 0.5 mol% in the presence of KO^{t}Bu, secondary amine **3a** was selectively afforded in 95% yield within 6 h (Table 3, entry 7). By using 1.0 equiv. of KOH and performing the reaction for 6 h, product **4a** was obtained in an 84% yield in 6 hours with 0.5 mol% of the **Ru1** catalyst (Table 3, entry 8). In our optimization studies, we observed that reducing the base below 2 equivalents significantly decreased the efficiency of the reaction, likely due to insuffi-

cient generation of the active Ru-alkoxide/Ru-hydride species, and there is no complete conversion of the starting material. Under these conditions, incomplete conversion of azobenzene was consistently observed, resulting in lower yields of the desired product (Table 3, entries 27 and 28). Also, excessively high base concentrations can also lead to side reactions or over-reduction, potentially decreasing selectivity. Thus, two equivalents of a strong base are required when using benzyl alcohols to ensure efficient deprotonation of the alcohol and the generation of the active Ru-alkoxide/Ru-hydride species. The first equivalent deprotonates the alcohol to form the alkoxide, which coordinates to the Ru center and facilitates hydride transfer to the azo compound. The second equivalent serves to neutralize the acidic byproducts formed during the dehydrogenation and *N*-alkylation steps, maintaining the catalytic cycle and promoting complete conversion.

Using less than two equivalents results in slower formation of the active species and lower conversion or selectivity toward the desired secondary amine or imine products. Without a catalyst or base, the reaction did not proceed, suggesting that both (catalyst and base) are crucial for the reaction (Table 3, entries 9 and 10). Then the reaction of azobenzene (0.5 mmol) with benzyl alcohol (1.1 mmol) was carried out in the presence of NaOH (1 mmol.) with 0.5 mol% of **Ru1** in toluene, selectively producing imine **4a** in 94% yield within 6 h (Table 3, entry 13). The choice of base strongly influences product selectivity in the dehydrogenative coupling of azobenzene with benzyl alcohol. Strong, non-nucleophilic bases such as KO^{t}Bu promote rapid alcohol deprotonation and Ru-hydride generation, thereby favoring the formation of the secondary amine (**3a**) *via* successive *N*-alkylation (entries 5, 7 and 26). In contrast, hydroxide bases like NaOH favor the formation of the imine (**4a**) by enabling more controlled hydride transfer and suppressing over-alkylation (entry 13). This divergence arises from differences in base strength and steric profile, which modulate both the efficiency of alcohol activation and the competition between imine accumulation and further conversion to the secondary amine.

Low catalyst loading of **Ru1** led to less conversion of azobenzene (Table 3, entries 15–18), whereas the reaction was ineffective at a temperature below 90 °C. We attempted the coupling of azobenzene (0.5 mmol) with benzyl alcohol (1.5 mmol) using 0.5 mol% of **Ru1** catalyst and KO^{t}Bu as a base (1 mmol) at 110 °C in toluene. The **Ru1** catalyst exhibited high selectivity, leading to the formation of secondary amine **3a** in 95% yield within 6 hours.

The catalyst screening was conducted for **Ru1–Ru5** complexes. The model reaction using 0.5 mol% of bimetallic **Ru3–Ru5** catalysts afforded **4a** in 86%, 89% and 94% yields respectively in the presence of NaOH (Table 3, entries 21–23). However, 1 mol% of monometallic **Ru2** yielded only 57% of **4a** (Table 3, entry 19). Furthermore, the model reaction with 0.5 mol% loading of **Ru3–Ru5** afforded **3a** in 86%, 91% and 94% yields respectively using KO^{t}Bu as the base (Table 3, entries 24–26). The reaction did not produce the desired product with [Ru(*p*-cymene)(μ-Cl)Cl]$_2$ (Table 3, entry 20). Conclusively, here the bimetallic catalyst outperforms the monometallic one in terms of catalytic activity, which is attributed to the cooperative effect of the bimetallic complex. In summary, we have uncovered two distinct sets of reaction conditions: *Condition A*: azo to secondary amine: benzyl alcohol (1.5 mmol), azo compound (0.5 mmol), KO^{t}Bu (1 mmol), toluene (1.0 mL), 100 °C, **Ru1** (0.5 mol%), 6 h; and *Condition B*: azo to imine: benzyl alcohol (1.1 mmol), azo compound (0.5 mmol), NaOH (1 mmol), toluene (1 mL), 100 °C, **Ru1** (0.5 mol%), 6 h.

4.1 Scope for azobenzene to secondary amines

With the optimized reaction conditions (optimal condition A) in hand for the coupling of azo compounds with benzyl alcohols, we delved into the synthesis of secondary amines from substituted azoarenes and benzyl alcohol (Scheme 5). The effect of substituents on reactivity and product formation was studied by varying substituents either on azobenzene or benzyl alcohols. Alkoxy, fluoro, chloro and bromo functionalities were found to be tolerated at the *p*-position of the aromatic ring of azobenzene, providing the secondary amines (**3b–3g**) in good yields.

Electron-rich *para*-substituted azoarenes such as methyl (**1b**), methoxy (**1c**) and isopropyl (**1d**) produced the desired secondary amines **3b** (96%), **3c** (92%) and **3d** (99%) in excellent yields. On the other hand, electron-deficient azoarenes such as –Br (**1e**), –Cl (**1f**) and –F (**1g**) substituted ones give relatively low yields of **3e** (87%), **3f** (84%) and **3g** (79%) secondary amines. The dehydrogenative reaction was sluggish when electron-deficient azoarene compounds were used. This could be attributed to either the weak coordinating ability of azo towards the ruthenium center or the low nucleophilicity of the resulting aniline, hindering the formation of secondary amines.

Next, we have explored the substrate scope for different benzyl alcohol derivatives with azobenzene. Diverse secondary amines were obtained through the reaction of azobenzene with a series of benzyl alcohols. The reactivity of benzyl alcohols with electron-rich substituents was favorable, while the electron-deficient and sterically demanding ones exhibited lower reactivity. The benzyl alcohols having –Me and –OMe at the *p*-position deliver the desired products **3h** (89%) and **3i** (92%) efficiently in high yields (Scheme 5). The benzyl alcohols having the *para*-CN substituent reacted effectively to produce the respective secondary amine **3j** in 87% yield. While halo-substituted benzyl alcohols reacted slowly and produced the desired secondary amines **3k** (72%), **3l** (82%), **3m** (86%) and **3n** (90%) in good yields, sterically hindered *ortho*-benzyl alcohol afforded **3o** in 71% yield. The *para*/*meta*-disubstituted benzyl alcohols provide the desired secondary aminated products **3p** and **3q** in 89% and 93% yields.

4.2 Scope for azobenzene to imines

After successfully exploring the selective synthesis of secondary amines, next, we focused on the selective synthesis of imines *via* coupling of benzyl alcohols with azoarenes under optimal reaction conditions (optimal conditions B: benzyl alcohol

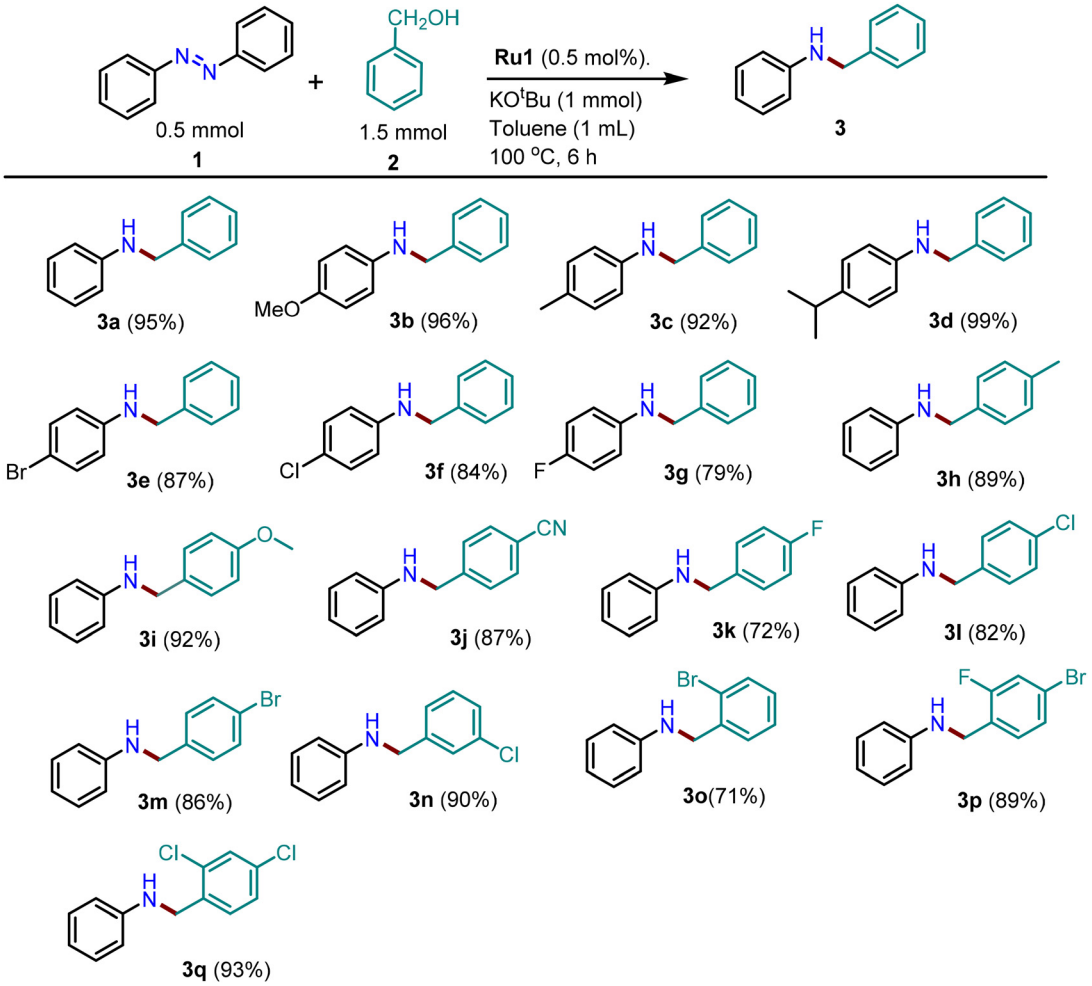

Scheme 5 Substrate scope for secondary amines.

(1.1 mmol), azoarenes (0.5 mmol), NaOH (1 mmol), toluene (1 mL), 100 °C, **Ru1** (0.5 mol%), 6 h). As shown in Scheme 6, various azobenzene and benzyl alcohol derivatives have been explored for the selective synthesis of imines.

The reaction of electron-rich azoarenes such as *para*-substituted ones (–Me and –OMe) produce the desired products **4b** and **4c** in 89%, and 92% yields respectively. The relatively low selectivity with halo-substituted substrates such as –F, and –Cl azoarenes can be attributed to the poor coordinating ability of the azo group with metal centers or its tendency to reduce the nucleophilicity of the *in situ* generated anilines. The effect of substituents on benzyl alcohols is also investigated using the coupling of different benzyl alcohols with azobenzene. The electron-rich benzyl alcohol performed well to obtain selective imines **4f** in 91% yield. On the other hand, electron-withdrawing *para*-substituents such as –CN and *para*-halogens on benzyl alcohols result in relatively low yields of the desired **4g–4j** imines. Disubstituted benzyl alcohols produce the corresponding imines **4k** and **4l** in 90% and 93% yields, respectively. This enhanced reactivity of disubstituted benzyl alcohols can be due to the inductive effects (Scheme 6).

The efficiency of the **Ru1** catalyst was demonstrated by calculating TONs and TOFs for the reaction of benzyl alcohol between azobenzene in the presence of KO^{t}Bu with 0.001 mol% of **Ru1** which gives a TON and TOF of 58 000 and 9666 h^{-1} respectively (Table 3, entry 18). Gram-scale reactions demonstrate that the present **Ru1**-catalyzed approach is easily scalable for the synthesis of secondary amines. As shown in Scheme 7, starting from 0.91 g (5 mmol) of azobenzene and 1.62 g of benzyl alcohol (15 mmol) in the presence of KO^{t}Bu, 1.63 g of the secondary amine **3a** (89%) is obtained with a catalyst loading of 0.5 mol% of **Ru1** (Fig. S19).

5. Mechanistic study: control experiments

To explore the mechanistic pathway for coupling azobenzene with alcohols using a hydrogen borrowing strategy, a series of control experiments were conducted. The catalyst loading was varied to understand the effect of catalyst loading on the selectivity of the catalyst for imine or secondary amine for-

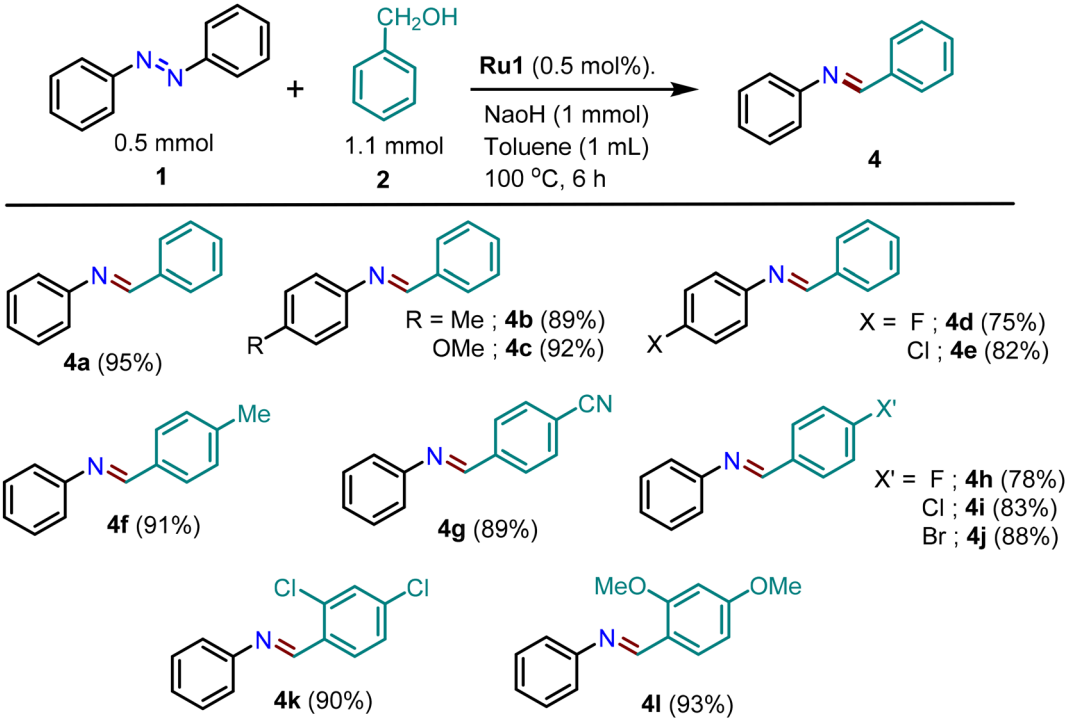

Scheme 6 Substrate scope for the formation of imines.

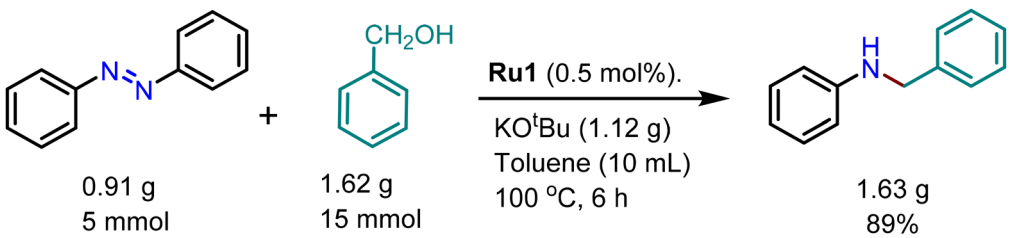

Scheme 7 Scale up reaction.

mation (Table 3). When the catalyst loading was decreased from 0.1 mol% to 0.001 mol% in the presence of KO^{t}Bu, the selectivity for the formation of secondary amines was decreased to 58% (Table 3, entry, 18). Similarly, by lowering the catalyst loading from 0.5 mol% to 0.001 mol% in the presence of NaOH, only a 39% yield of imine product was obtained (Table 3, entry 16). When the reaction was performed in the absence of a base or catalyst, no product formation was observed, demonstrating the important role of both catalyst and base (Scheme 8a and b). Furthermore, the dehydrogenation was confirmed by the reaction of benzyl alcohol (Scheme 8c) under optimized conditions in the presence of KO^{t}Bu, resulting in the formation of benzaldehyde *via* a dehydrogenation strategy (detected by GC-MS spectrometry). Under optimal conditions, the reaction between aniline with benzyl alcohol afforded a 95% yield of secondary amines (Scheme 8d and Fig. S20), whereas the same reaction in the presence of NaOH as a base gave a mixture of secondary amines (37%) and imines (61%). The use of tertiary butanol instead of benzyl alcohol as the coupling partner resulted in no observable reaction. This observation highlights the necessity of having an α-hydrogen present in the reactants for successful dehydrogenation and product formation (Scheme 8e). Furthermore, to verify whether imines are intermediates in amine synthesis, we performed the optimal reaction and monitored it using GC-MS. These studies show that imine species form initially and their concentration decreases as the reaction progresses, while the corresponding amine product increases, consistent with the imine acting as a transient intermediate (Scheme 8f and Fig. S108). These observations confirm that imines serve as key intermediates in the formation of secondary amines in our catalytic system.

All the above observations indicate the formation of an aldehyde and aniline intermediate from the alcohol and azobenzene *via* dehydrogenation and hydrogenation respectively during the catalytic process. The process involved the conden-

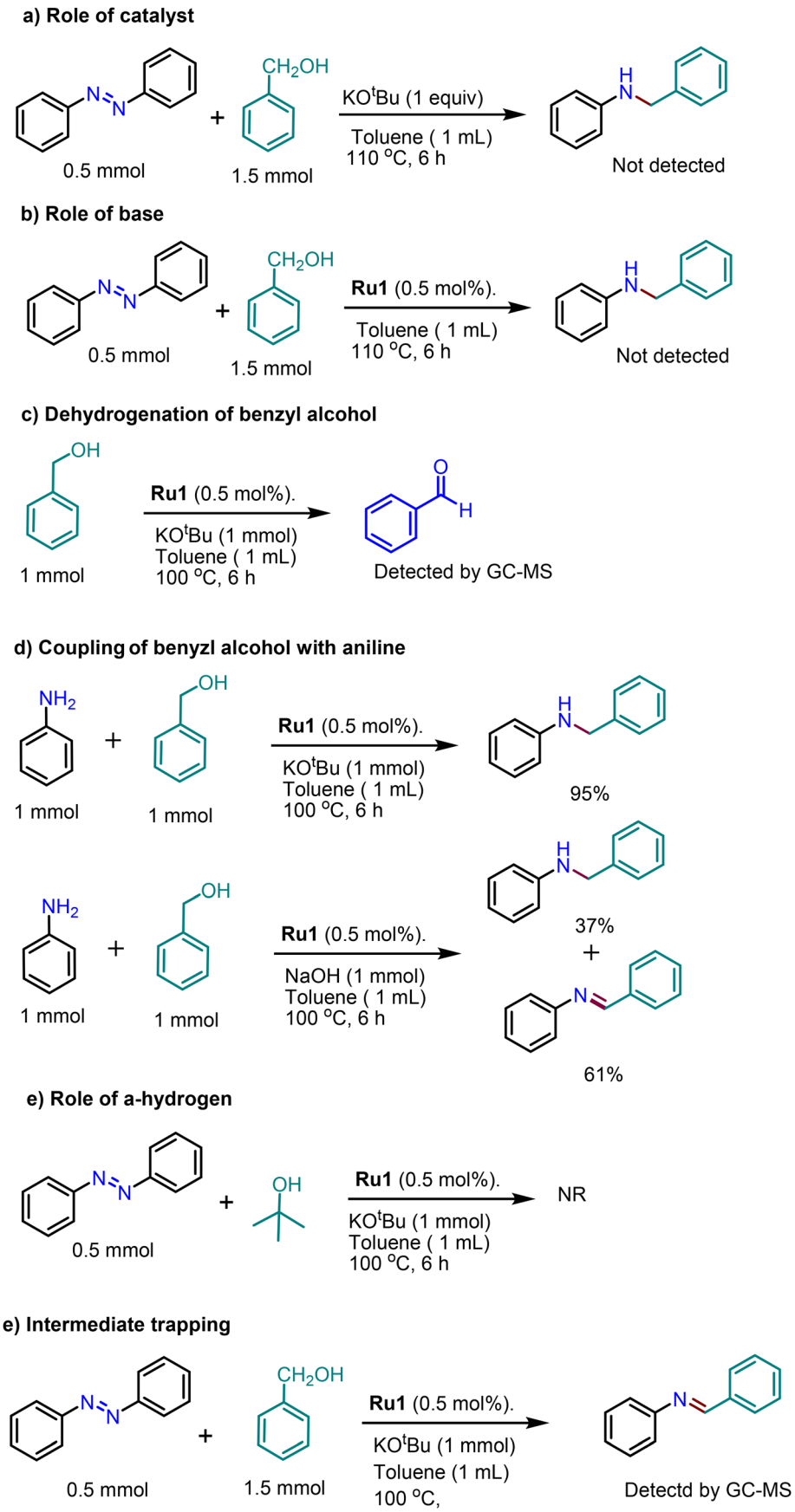

Scheme 8 Control experiments.

sation of an aldehyde with an amine, leading to the formation of an imine. This imine was then subsequently reduced by Ru-hydride species, which were generated through the dehydrogenation of Ru-alkoxide (Fig. 8). The reduction of the imine resulted in the formation of the desired secondary amine product. Therefore, the overall process can be described by the following hydrogen borrowing pathway.

5.1 Mechanistic study using DFT

The electronic structure of the optimized geometry of catalyst **Ru5** is similar to **Ru1** which has already been reported in a previous study.[37] Based on the experimental findings described above and previously reported mechanisms for similar reactions, we have adopted the following mechanism for coupling

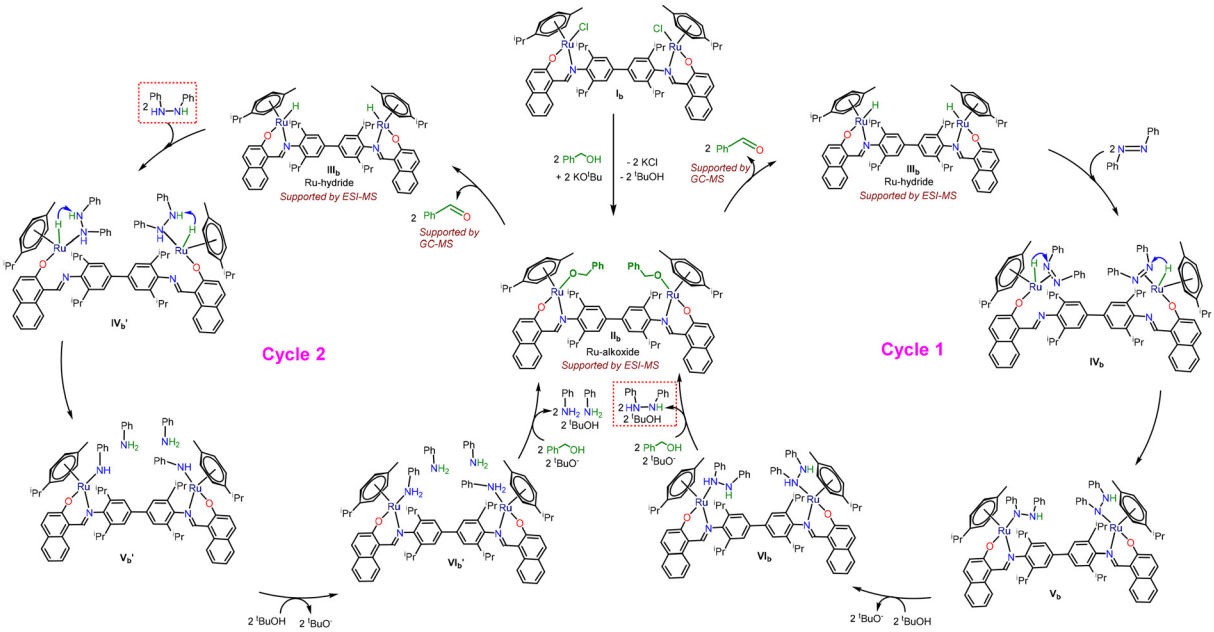

Fig. 9 Catalytic cycle for coupling of azobenzene with benzyl alcohol.

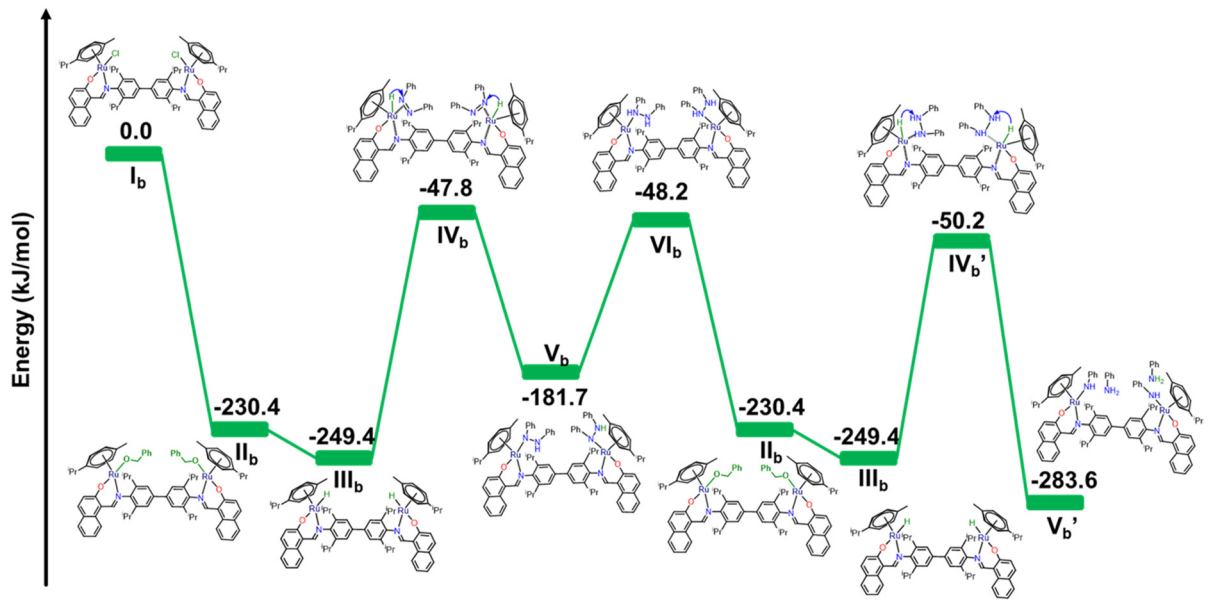

Fig. 10 The computed potential energy profile diagram in solvent phase free energies (ΔG), at the B3LYP-D3/def2-TZVP level of theory for reaction pathways of the bimetallic complex.

azo compounds with benzyl alcohol (Fig. 9).[24,30] In the first step, **Ru5** (species $\mathbf{I_b}$) undergoes chloride ion exchange with a benzyloxide ion (formed *via* deprotonation of benzyl alcohol with a base), resulting in the formation of Ru-benzyloxide species $\mathbf{II_b}$ (benzyloxide-coordinated ruthenium intermediate; detected by ESI-MS corresponding to the $[M + H]^+$ ion at *m*/*z* 1389.993 (Fig. S22)) which is found to be exothermic by 230.4 kJ mol^{-1}. Species $\mathbf{II_b}$ undergoes β-hydride elimination to form a Ru-hydride species ($\mathbf{III_b}$) *via* the elimination of benzaldehyde and this step is found to be 19 kJ mol^{-1} exothermic with respect to species $\mathbf{II_b}$. The Ru-hydride species ($\mathbf{III_b}$) was also detected using ESI-MS at *m*/*z* 1156.987, corresponding to the $[M + Na]^+$ ion (Fig. S23). The protonation of the phenoxy group (Ru–OAr) which leads to the dissociation of Ru–O(H)Ar and generation of a cationic Ru(II) intermediate is also considered. However, this cationic species is energetically less favourable: the protonated Ru–O(H)Ar dissociation product is higher in energy by 15.4 kJ mol^{-1} compared to the Ru–N bond-cleaved intermediate. In the next step, the nitrogen atom in the Schiff-base ligand, which is coordinated to the metal center, undergoes dissociation. This dissociation reduces the coordination number of the metal center, leading to the formation of a 16-electron (16e$^-$) intermediate and its formation is estimated to be endothermic from species $\mathbf{III_b}$. This 16e$^-$ species establishes a strong η^2 interaction with the N=N (azo bond) group without any energy barrier. This interaction facilitates the reorganization of the system and, ultimately, formation of species $\mathbf{IV_b}$ endothermically by 201.6 kJ mol^{-1} (Fig. 10). Afterward, hydride migrates from Ru to the nitrogen atom of the azo group and species $\mathbf{V_b}$ is formed exothermically by 133.9 kJ mol^{-1}. The interaction of the azo compound with the counter cation of the base leads to polarisation of the N=N bond, which lowers the hydride transfer barrier by approximately 3 kJ mol^{-1}. This stabilisation arises from enhanced polarisation of the azo functionality, increasing its electrophilic character and facilitating the hydride transfer step. These results suggest that while the Ru-OAr protonation/dissociation pathway is energetically disfavoured, weak interactions of the azo compound with cations provide a subtle but important reduction in the hydride transfer barrier, thereby contributing to the observed reactivity. In the next step, the second nitrogen atom of the azo group is protonated by the acid buffer added to the reaction. This is accompanied by the release of phenylhydrazine with the reaction being endother-

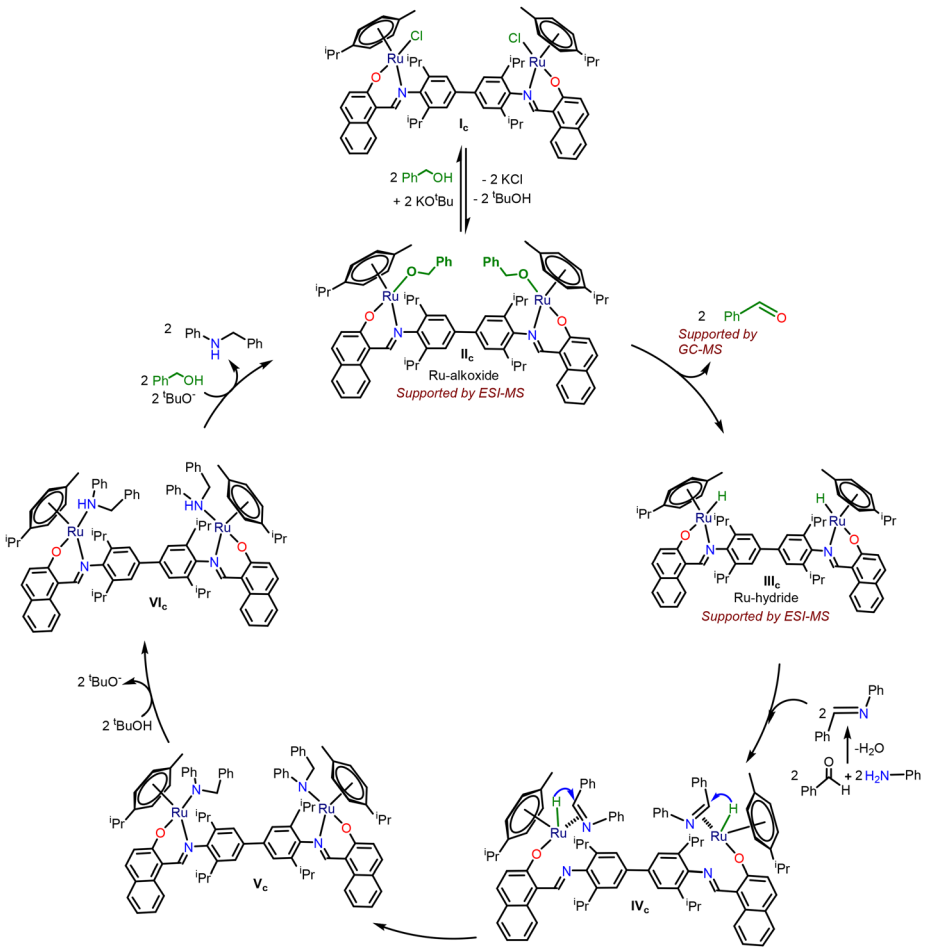

Fig. 11 Probable mechanism of hydrogenation of azobenzene using the **Ru5** catalyst.

mic by 133.5 kJ mol^{-1}. The process also regenerates species $\mathbf{II_b}$ from species $\mathbf{V_b}$, which is exothermic, indicating a favorable and efficient reaction. In the next step, phenylhydrazine coordinates with the metal center in species $\mathbf{III_b}$ to form intermediate $\mathbf{IV_b}'$, and the HN═NH bond is subsequently hydrogenated by hydrogen transfer to generate the coordinated amine intermediate $\mathbf{V_b}'$ which releases aniline as a product.

The aniline formed as a product, along with benzaldehyde generated *via* hydride transfer, undergoes condensation to yield an imine intermediate. This imine subsequently coordinates with the ruthenium–hydride species ($\mathbf{III_c}$), resulting in the formation of intermediate $\mathbf{IV_c}$, as shown in Fig. 11. A subsequent hydride transfer from the ruthenium metal center to the carbon atom of the imine leads to the formation of species $\mathbf{V_c}$ (Fig. 11). Finally, in the presence of a buffer solution acting as a proton source, protonation of $\mathbf{V_c}$ results in the corresponding secondary amine (Fig. 12).

The same catalytic pathway has been observed for coupling of azoarenes with benzyl alcohol using **Ru1** and **Ru4** complex. The detection of the intermediate species Ru-alkoxide has been successfully probed using ESI-MS studies. The Ru-alkoxide shows a molecular ion peak corresponding to the $[M + H]^+$ ion at *m*/*z* 1277.617 (Fig. S24) for **Ru1** and at *m*/*z* 1639.834 for **Ru4** (Fig. S25).

To understand the experimentally observed rate difference between **Ru5** and **Ru2**, calculations were also performed for monometallic species, as shown in Fig. 13. The results reveal a distinct reactivity pattern for **Ru5**, characterized by the enhanced stability of intermediates, evident from their larger exothermic formation energies. Additionally, the statistical probability of reactivity is higher for **Ru5**, as it contains two active metal centers. The critical step in the reaction mechanism that influences kinetics occurs between species **IIIa** and **IVa** (Fig. 13). During this step, the nitrogen atom of the Schiff-base ligand, coordinated to the metal center, dissociates, reducing the coordination number and forming a reactive 16-electron (16e$^-$) intermediate. The transition state leading to this species has an energy barrier of 92.8 kJ mol^{-1} from species **III**, indicating substantial kinetic hindrance. This 16e$^-$ intermediate is inherently unstable, making it highly reactive as it readily binds with an additional ligand in the subsequent step.

In **Ru5**, the metal center establishes a strong η^2 interaction with the azo (N═N) group without any energy barrier, facilitating system reorganization and the formation of species **IV**. Natural bond orbital (NBO) analysis reveals differences in charge distribution between **Ru2** and **Ru5**. In **Ru5**, the nitrogen atom of the 16e$^-$ species carries a natural charge of −0.203/−0.201, compared to a slightly more negative charge of −0.211 in **Ru2**. This charge delocalization in **Ru5** suggests greater electron sharing and enhanced metal–ligand interactions, promoting faster reactions. Computational studies further indicate that the 16e$^-$ intermediate in **Ru4** is 44.5 kJ mol^{-1} more stable than its monometallic counterpart. In the monometallic Ru(II) complex, the charge localised on the Ru centre is 0.407, whereas in the bimetallic systems, the charges

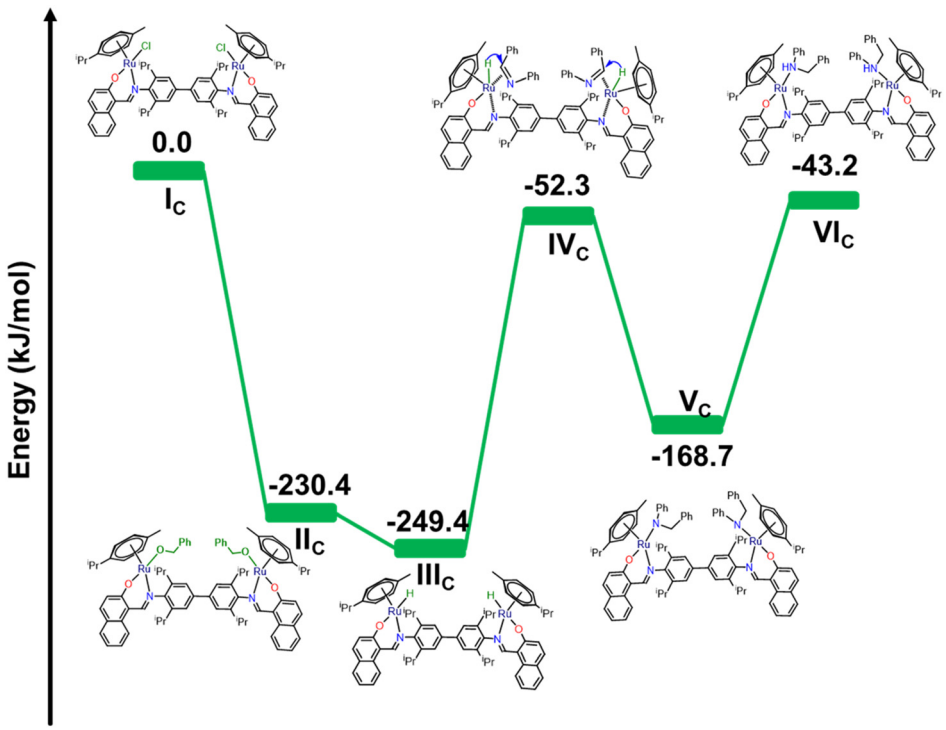

Fig. 12 The computed potential energy profile diagram in solvent phase free energies (ΔG), at the B3LYP-D3/def2-TZVP level of theory for reaction pathways of the bimetallic complex.

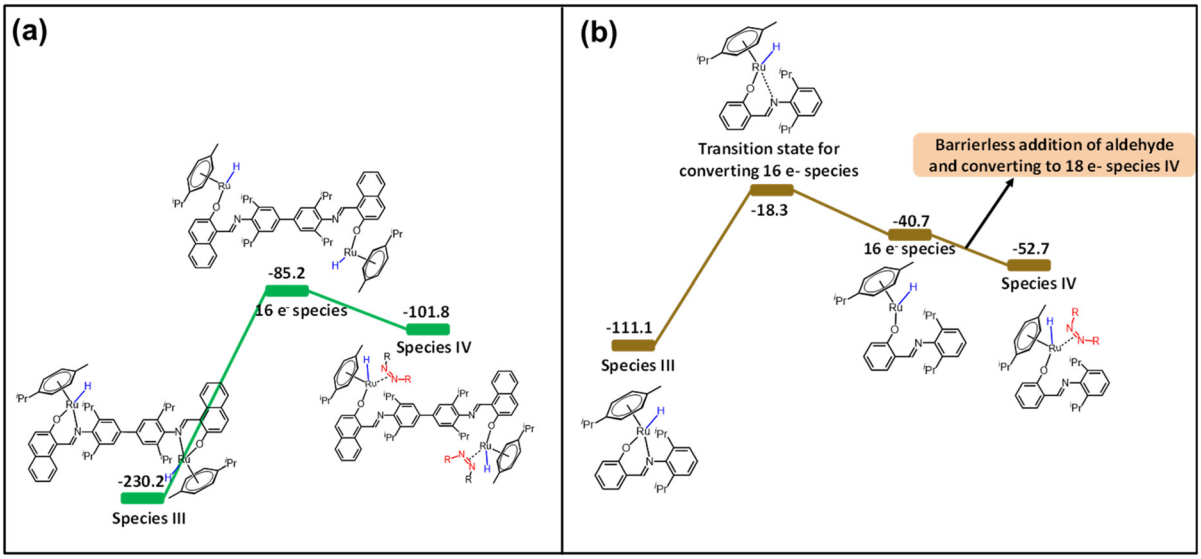

Fig. 13 The comparison of kinetics for the rate determining step of the reaction, computed at the B3LYP-D3/def2-TZVP level of theory for **Ru5** (a) and **Ru2** (b).

are more evenly delocalized between the two Ru centres (0.390/0.388). This indicates that electronic communication in the bimetallic framework reduces the electron density at each Ru atom. These findings support the presence of cooperativity in **Ru5** and its absence in **Ru2**, explaining the observed variation in reactivity rates. The increased stability of the bimetallic complex aligns with experimental trends, where **Ru5** is more reactive due to better stabilization and its readiness to partici-

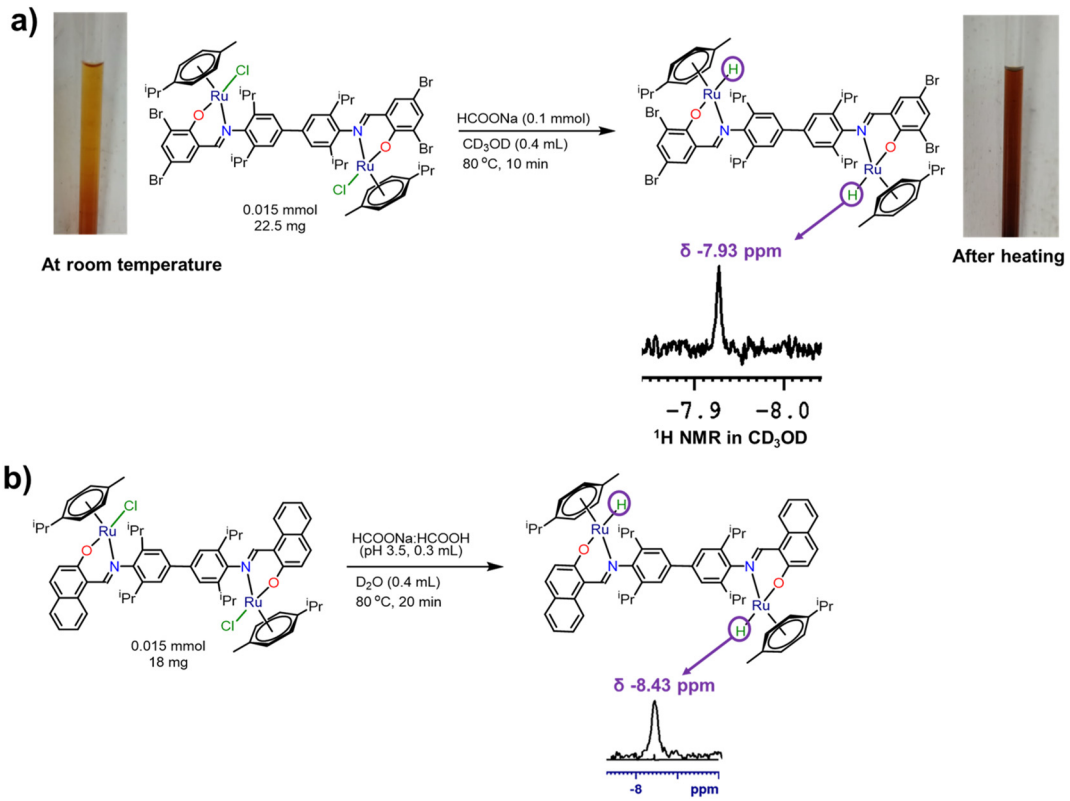

Fig. 14 Detection of ruthenium–hydride species using ^{1}H NMR spectroscopy: (a) reaction mixture of sodium formate with **Ru4** and (b) reaction mixture of formate buffer (pH 3.5) with **Ru5**.

pate in subsequent reaction steps. These results demonstrate the complementary nature of bimetallic reactivity, consistent with experimental observations.

5.2 Detection of ruthenium–hydride species by NMR spectroscopy

To identify ruthenium–hydride species in a reaction mixture, an NMR experiment was performed. An NMR tube was prepared containing **Ru4**/**Ru5** (0.015 mmol), 0.4 mL of deuterated water, and either 0.1 mmol of sodium formate or 0.3 mL of buffer (pH 3.5). The mixture was then heated at 80 °C for 10–20 minutes. ^{1}H NMR spectroscopy analysis showed a distinct peak at δ −7.93 ppm for **Ru4**, while a weak signal appeared at δ −8.43 ppm for **Ru5**, confirming the formation of a ruthenium–hydride species (Fig. 14 and Fig. S29, S30). Additionally, a noticeable color shift from pale yellow to dark brown suggested the conversion of Ru complexes into the Ru-hydride intermediate.

6. Conclusions

The activated N=N azo bond being used as a nitrogen source for value-added products is the key aspect of the methodology described in this investigation, which allows the versatile synthesis of anilines, secondary amines, and imines by using a single substrate and catalyst system. The chemoselective TH of azoarenes in water with Ru(II) catalysts using formic acid/formate buffer as a hydride source has been demonstrated under mild reaction conditions with a low catalyst loading of 0.01 mol%. Furthermore, dehydrogenative coupling of azoarenes with benzyl alcohol leads to the selective synthesis of secondary amines or imines using 0.5 mol% of a binuclear Ru(II) catalyst. The present catalytic approach is operationally simple and functions under mild conditions facilitating its application in both aqueous and organic solvents. Its broad substrate scope and excellent compatibility with various functional groups render it highly adaptable for large-scale processes. Combined evidence from NMR and mass (ESI) spectroscopic studies and DFT calculations reveal that the Ru(II) catalyst promotes azo bond activation *via* a hybrid-model complex. Detailed DFT calculations elucidated the mechanistic pathway of breaking of the azo bond and investigated the origin of the superior reactivity of the **Ru5** catalyst relative to the **Ru2** catalyst. The computational results suggest that the observed enhancement in catalytic activity for the dinuclear **Ru5** system may be attributed, at least in part, to cooperative effects operating between the two metal centers.

7. Experimental section

7.1 Materials, physical measurements and instruments

Starting materials such as 2,2′,6,6′-tetraisopropylbenzidine (TIBZ),[46] Schiff base ligands $\mathbf{H_2L^1}$–$\mathbf{H_2L^3}$,[42,43] [Ru(*p*-cymene)(μ-Cl)Cl]$_2$,[47] and complexes **Ru1**–**Ru3** [37,41] were prepared according to the reported procedures. Ruthenium(III) trichloride trihydrate (Sigma-Aldrich), α-phellandrene, salicylaldehyde and 5-bromosalicylaldehyde (Sigma Aldrich), bromine (Spectrochem), 2,6-diisopropylaniline (Alfa Aesar), and benzaldehyde (Spectrochem) were used as received. Other substrates and analytical grade solvents were procured commercially and used without further purification. The ruthenium compounds reported herein are air and moisture-stable. The elemental analyses reports of $\mathbf{H_2L^4}$, $\mathbf{H_2L^5}$, **Ru4** and **Ru5** are given in the SI (Fig. S102–S105)

All the experiments were carried out in a well-ventilated fume hood under ambient reaction conditions. The ^{1}H and ^{13}C NMR spectra were recorded on a Bruker AV III 400 MHz NMR spectrometer using $CDCl_3$ or DMSO-d_6 as the solvent. Melting points were measured in glass capillaries and are reported uncorrected. FT-IR spectra were recorded on a PerkinElmer Spectrum One infrared spectrometer (model number 73465) as KBr diluted discs in the frequency range of 4000–400 cm^{-1}. Elemental analyses were performed on a Thermo Finnigan (FLASH EA 1112) microanalyzer. ESI-MS measurements were performed on a Bruker Maxis Impact electrospray mass spectrometer. A UV-NIR-3600 spectrophotometer from Shimadzu was used for the UV-visible studies. An Agilent 7890A GC system with an FID detector and a J & W DB-1 column (10 m, 0.1 mm ID) were used to conduct GC-MS analysis.

Suitable single crystals of $\mathbf{H_2L^4}$, $\mathbf{H_2L^5}$, **Ru4** and **Ru5** were grown directly from the crude products for X-ray diffraction analysis. Low-temperature single crystal X-ray diffraction intensity data were collected using a BRUKER D8 QUEST diffractometer equipped with an IμS DIAMOND microfocus Mo-Kα radiation source (λ = 0.7107 Å). Data integration and indexing were performed using the CrysAlisPro software suite.[48] All calculations were carried out using the programs in the WinGX module and Olex 2-1.3.[49,50] Refinement of the structures employed full least-squares methods on F^2 with SHELXL-2014, refining all non-hydrogen atoms anisotropically.[51] Crystal data and structure refinement details for $\mathbf{H_2L^4}$, $\mathbf{H_2L^5}$, **Ru4** and **Ru5** are given in Tables S2–S6.

7.2 Computational details

All DFT calculations have been performed using the Gaussian16.C suite of programs.[52] The methodology that has been used is the B3LYP-D3 functional along with the basis set LANL2DZ for Ru atoms and 6-31G* for other atoms.[53] This is a time-tested methodology for the Ru catalyst and has also reproduced several experimental spectral features, offering confidence in the methodology. The single point energies were computed on the optimized geometries using the def2-TZVP basis set for all atoms.[54] The Gibbs free energy correction has been added to the single point energies obtained from the higher basis set to refine the gas phase electronic energies. The solvation has been modeled using the solvent model density (SMD), using water and toluene as the solvent.[55] The geometrical parameters obtained from the optimized structure of catalysts **Ru4** and **Ru5** are in agreement with the single-

crystal X-ray diffraction data (Table S7). The natural bonding orbitals (NBO) analysis has been performed using the same methodology.[56]

7.3 Synthesis of H_2L^4 and H_2L^5

In a round bottomed flask, TIBZ (0.63 g, 1.6 mmol) was dissolved in methanol (50 mL). To this solution, 3,5-dibromo salicylaldehyde (0.89 g, 3.2 mmol) or 2-hydroxy-1-naphthaldehyde (0.54 g, 3.2 mmol) and a catalytic amount of formic acid (3–4 drops) were added under stirring. The reaction mixture was refluxed for 12 hours to obtain a yellow precipitate, which was collected by filtration and washed with cold methanol 2–3 times. **H_2L^4** or **H_2L^5** was obtained as a yellow crystalline solid in high yield by recrystallization of the yellow residue from a mixture of methanol and dichloromethane (3 : 2 v/v).

For **H_2L^4**: yield (85%, 1.14 g), mp >280 °C. Anal. calc. for $C_{38}H_{40}Br_4O_2N_2$; C, 52.08; H, 4.60; N, 3.20. Found: C, 52.48; H, 4.79; N, 2.75; ESI-MS: $[M + H]^+$ = 876.970 (Mr 875.366) *m/z*; ^{1}H NMR (400 MHz, $CDCl_3$) δ 14.0 (s, 2H), 8.27 (s, 2H), 7.82 (d, $^4J_{H,H}$ = 2.3 Hz, 2H), 7.47 (d, $^4J_{H,H}$ = 2.3 Hz, 2H), 7.31 (s, 4H), 3.01 (sept, $^3J_{H,H}$ = 6.8 Hz, 4H), 1.25 (d, $^3J_{H,H}$ = 6.8 Hz, 24H) ppm. ^{13}C NMR (101 MHz, $CDCl_3$) δ 165.12, 157.41, 144.28, 139.60, 139.26, 138.46, 133.56, 122.52, 120.21, 112.32, 110.46, 28.43, 23.46 ppm. FT-IR (KBr diluted pellet, cm^{-1}) 3428 (b), 3023 (s), 2964 (s), 1640 (s), 1605 (s), 1510 (s), 1493 (s), 1421 (s), 1414 (w), 1311 (w), 1239 (s), 1207 (s), 1116 (s), 1028 (w), 908 (s), 829 (s), 710 (w). UV-Vis (dichloromethane, λ_{max} (nm), ε ($\times 10^5$ M^{-1} cm^{-1})) 234 (2.3), 276 (1.8), 354 (0.3).

For **H_2L^5**: yield (97%, 1.06 g), mp 281 °C. Anal. calc. for $C_{46}H_{48}O_2N_2$; C, 83.60; H, 7.32; N, 4.24. Found: C, 83.06; H, 7.13; N, 3.91; ESI-MS: $[M + H]^+$ = 661.325 (Mr 660.902) *m/z*; ^{1}H NMR (400 MHz, $CDCl_3$) δ 9.15 (s, 2H), 8.02 (d, $^3J_{H,H}$ = 8.2 Hz, 2H), 7.97 (d, $^3J_{H,H}$ = 9.2 Hz, 2H), 7.83 (d, $^3J_{H,H}$ = 8.0 Hz, 2H), 7.56 (t, $^3J_{H,H}$ = 7.4 Hz, 2H), 7.47 (s, 4H), 7.49–7.43 (m, 4H), 3.21 (sept, $^3J_{H,H}$ = 6.8 Hz, 4H), 1.35 (d, $^3J_{H,H}$ = 6.8 Hz, 24H) ppm. ^{13}C NMR (101 MHz, $CDCl_3$) δ 167.49, 162.15, 141.31, 140.29, 139.47, 133.09, 129.65, 128.67, 127.66, 123.96, 122.86, 120.92, 118.74, 28.65, 23.79 ppm. FT-IR (KBr diluted pellet, cm^{-1}) 3367 (b), 2969 (s), 2891 (w), 1631 (s), 1574 (s), 1497 (w), 1456 (s), 1406 (s), 1323 (s), 1287 (s), 1235 (w), 1179 (s), 1150 (s), 1109 (w), 1085 (w), 911 (s), 867 (s), 790 (s), 763 (s), 687 (s). UV-Vis (dichloromethane, λ_{max} (nm), ε ($\times 10^5$ M^{-1} cm^{-1})) 230 (3.1), 271 (1.8), 348 (0.9).

7.4 Synthesis of Ru4 and Ru5

H_2L^4 (87.6 mg, 0.1 mmol) or **H_2L^5** (66 mg, 0.1 mmol) and potassium carbonate (28 mg, 0.2 mmol) were mixed in ethanol (30 mL), and to this mixture $[Ru(p\text{-cymene})(\mu\text{-}Cl)Cl]_2$ (61 mg, 0.1 mmol) was added under stirring. The color of the reaction mixture changed from yellow to dark red indicating the progress of the reaction. The reaction mixture was stirred vigorously at room temperature overnight and the solvent was removed under vacuum, leaving the crude **Ru4** or **Ru5** as a dark residue in high yield. The residue was dissolved in dichloromethane and filtered through Celite, and the solvent was evaporated to obtain a red residue in each case which on recrystallization from a mixture of dichloromethane and ethanol (10 : 1 v/v) produced analytically pure samples of **Ru4** and **Ru5**.

For **Ru4**: yield (119 mg, 84%), mp >250 °C. Anal. calc. for $C_{58}H_{66}N_2O_2Cl_2Br_4Ru_2$; C, 49.20; H, 4.70; N, 1.98. Found: C, 49.04; H, 4.14; N, 1.65; ESI-MS: $[M + CH_3CN + H]^+$ = 1457.979 (Mr = 1411.932). ^{1}H NMR (400 MHz, $CDCl_3$) δ 7.62 (d, $^3J_{H,H}$ = *2.5* Hz, 2H), 7.59 (s, 2H), 7.53 (s, 2H), 7.42 (s, 2H), 6.90 (d, $^3J_{H,H}$ = 2.6 Hz, 2H), 5.51 (d, $^3J_{H,H}$ = 5.1 Hz, 2H), 5.41 (d, $^3J_{H,H}$ = 6.3 Hz, 2H), 5.09 (d, $^3J_{H,H}$ = 6.3 Hz, 2H), 4.44 (d, $^3J_{H,H}$ = 6.0 Hz, 2H), 4.18 (sept, $^3J_{H,H}$ = 6.6 Hz, 2H), 3.27 (sept, 6.7 Hz, 2H), 3.00 (sept, $^3J_{H,H}$ = 6.9 Hz, 2H), 1.97 (s, 6H), 1.59 (d, $^3J_{H,H}$ = 6.9 Hz, 6H), 1.50 (d $^3J_{H,H}$ = 6.7 Hz, 6H), 1.43 (d, $^3J_{H,H}$ = 6.9 Hz, 6H), 1.33 (d, $^3J_{H,H}$ = 6.9 Hz, 6H), 1.15 (d, $^3J_{H,H}$ = 6.7 Hz, 6H), 1.09 (d, $^3J_{H,H}$ = 6.6 Hz, 6H) ppm. ^{13}C NMR (101 MHz, $CDCl_3$) δ 165.95, 162.36, 151.57, 142.98, 141.89, 140.19, 139.90, 135.49, 123.14, 122.10, 121.33, 117.81, 106.08, 104.45, 94.23, 87.98, 84.30, 82.04, 30.49, 28.14, 27.66, 26.79, 26.06, 23.18, 22.46, 22.18, 18.43, 17.74 ppm. FT-IR (KBr diluted pellet, cm^{-1}) 3077 (s), 3027 (s), 1621 (s), 1602 (w), 1501 (s), 1449 (ss), 1389 (w), 1332 (s), 1240 (s), 1167 (s), 1075 (s), 1015 (s), 956 (w), 749 (s) 786 (s). UV-Vis (dichloromethane, λ_{max} (nm), ε ($\times 10^5$ M^{-1} cm^{-1})) 264 (2.0), 457 (0.1).

For **Ru5**: yield (91 mg, 82%), mp >250 °C. Anal. calc. for $C_{66}H_{74}N_2O_2Cl_2Ru_2$; C, 66.04; H, 6.21; N, 2.33. Found: C, 65.29; H, 6.22; N, 1.91; ESI-MS: $[M - Cl]^+$ = 1165.347 (Mr = 1200.372). ^{1}H NMR (400 MHz, $CDCl_3$) δ 8.13 (s, 2H), 7.65 (s, 2H), 7.59 (d, $^3J_{H,H}$ = *9.3* Hz, 2H), 7.55 (d, $^3J_{H,H}$ = *6.6* Hz, 2H), 7.53(d, $^3J_{H,H}$ = 8.6 Hz, 2H), 7.49 (d, $^3J_{H,H}$ = 8.8 Hz, 2H), 7.26–7.23 (m, 2H) 7.16–7.09 (m, 2H), 5.47 (d, $^3J_{H,H}$ = 6.0 Hz, 2H), 5.41 (d, $^3J_{H,H}$ = 6.3 Hz, 2H), 4.94 (d, $^3J_{H,H}$ = 5.8 Hz, 2H), 4.38 (d, $^3J_{H,H}$ = 6.0 Hz, 2H), 4.33 (sept, $^3J_{H,H}$ = 6.7 Hz, 2H), 3.23 (sept, 6.6 Hz, 2H), 2.86 (sept, $^3J_{H,H}$ = 7.0 Hz, 2H), 2.08 (s, 6H), 1.55 (d, $^3J_{H,H}$ = 6.6 Hz, 12H), 1.45 (d $^3J_{H,H}$ = 7.0 Hz, 6H), 1.33 (d, $^3J_{H,H}$ = 6.9 Hz, 6H), 1.29 (d, $^3J_{H,H}$ = 6.6 Hz, 6H), 1.01 (d, $^3J_{H,H}$ = 6.9 Hz, 6H) ppm. ^{13}C NMR (101 MHz, $CDCl_3$) δ 167.70, 159.85, 152.93, 143.62, 142.71, 140.00, 135.92, 134.77, 128.90, 127.54, 126.67, 124.65, 122.87, 122.28, 121.96, 118.72, 110.31, 104.12, 94.44, 88.60, 84.45, 82.18, 30.94, 28.05, 27.67, 26.86, 26.28, 23.54, 23.15, 22.45, 21.74, 17.89 ppm. FT-IR (KBr diluted pellet, cm^{-1}) 3012 (s), 1625 (s), 1595 (s), 1578 (w), 1490 (s), 1436 (s), 1401 (s), 1324 (s), 1250 (s), 1188 (s), 1095 (w), 1041 (s), 987 (s), 947 (s), 870 (s), 768 (s). UV-Vis (dichloromethane, λ_{max} (nm), ε ($\times 10^5$ M^{-1} cm^{-1})) 225 (3.1), 269 (3.3), 324 (1.2), 450 (0.3).

7.5 General procedure for transfer hydrogenation of azo compounds to aniline

A flask containing a stir bar was loaded with **Ru1** or **Ru3–Ru5** (0.1 mol%) (or **Ru2**, 0.2 mol%), buffer solution (HCOONa : HCOOH, pH 3.5, 3 mL), and water (2 mL). The resultant mixture was stirred at 80 °C for 5 minutes and azoarene substrates (0.5 mmol) were added and stirred at 80 °C for 5 hours. GC-MS analysis was used to monitor the product formation. After completion of the reaction, the product was extracted with ethyl acetate and dried over sodium sulfate to obtain the desired aniline. The products have been further

purified by column chromatography using a petroleum ether–ethyl acetate mixture (95 : 5) as the eluent. The products were analyzed using NMR spectroscopy.

7.6 General procedure for the synthesis of secondary amines

An oven-dried 10 mL reaction tube was charged with the benzyl alcohol substrate (1.5 mmol) and KO^{t}Bu (112 mg, 1 mmol) in toluene (1 mL) and stirred for 10 minutes at 100 °C. After that, the **Ru1** or **Ru3–Ru5** catalyst (0.5 mol%) and the azo compound (0.5 mmol) were added. The resulting reaction mixture was further heated at 100 °C for 6 hours in a sealed tube. The progress of the reaction was monitored using GC-MS spectrometry. After completion of the reaction, the solvent was removed under vacuum. The products were further purified by column chromatography using a petroleum ether–ethyl acetate mixture (98 : 2) as the eluent. The products were analyzed using NMR spectroscopy.

7.7 General procedure for the synthesis of imines

A round bottomed flask containing a benzyl alcohol derivative (1.1 mmol) and NaOH (40 mg, 1 mmol) was stirred at 100 °C for 10 minutes in toluene (1 mL). Subsequently, the **Ru1** or **Ru3–Ru5** catalyst (0.5 mol%) and the azo compound (0.5 mmol) were added and stirred at 100 °C for 6 hours. After completion of the reaction, the solvent was removed under vacuum and the product was purified by column chromatography using a petroleum ether–ethyl acetate mixture (98 : 2) as the eluent. The products were analyzed using GC-MS and NMR spectroscopy.

Conflicts of interest

There are no conflicts to declare.

Data availability

The data supporting this article have been included as part of the SI. Supplementary information: experimental details, computational methods, ESI-MS, and NMR assignments supporting this study's findings. See DOI: **https://doi.org/10.1039/d5dt01813g**.

CCDC 2432945 (**H_2L^4**), 2432946 (**H_2L^5**), 2432947 (**Ru4**) and 2432948 (**Ru5**) contain the supplementary crystallographic data for this paper.[57a–d]

Acknowledgements

This work was supported by the SERB, New Delhi, through a J. C. Bose Fellowship grant to R. M. (SB/S2/JCB-85/2014). G. R. would like to acknowledge the SERB for funding (CRG/2022/001697; SB/SJF/2019-20/12). G. D. thanks CSIR/UGC, New Delhi, and IIT Bombay for a research fellowship. T. R. K. R. acknowledges the financial support from the Prime Minister's Research Fellowship (PMRF). The authors thank the IoE-funded central facilities and SAIF, IIT Bombay for help with various spectral measurements. The authors thank S. Bhuin for his help in experimental studies.

References

1 S. Kobayashi and H. Ishitani, *Chem. Rev.*, 1999, **99**, 1069–1094.
2 V. Froidevaux, C. Negrell, S. Caillol, J. P. Pascault and B. Boutevin, *Chem. Rev.*, 2016, **116**, 14181–14224.
3 D. Quo, H. Huang, J. Xu, H. Jiang and H. Liu, *Org. Lett.*, 2008, **10**, 4513–4516.
4 J. Wu and C. Darcel, *ChemCatChem*, 2022, **14**, e202101874.
5 Y. Pan, Z. Luo, X. Xu, H. Zhao, J. Han, L. Xu, Q. Fan and J. Xiao, *Adv. Synth. Catal.*, 2019, **361**, 3800–3806.
6 C. Wang, A. Pettman, J. Basca and J. Xiao, *Angew. Chem., Int. Ed*, 2010, **49**, 7548–7552.
7 E. W. Baxter and A. B. Reitz, *Organic Reactions*, John Wiley & Sons, Inc., 2002, vol. 59, pp. 1–714.
8 O. I. Afanasyev, E. Kuchuk, D. L. Usanov and D. Chusov, *Chem. Rev.*, 2019, **119**, 11857–11911.
9 T. Irrgang and R. Kempe, *Chem. Rev.*, 2020, **120**, 9583–9674.
10 V. R. Jumde, L. Gonsalvi, A. Guerriero, M. Peruzzini and M. Taddei, *Eur. J. Org. Chem.*, 2015, 1829–1833.
11 E. Podyacheva, O. I. Afanasyev, D. V. Vasilyev and D. Chusov, *ACS Catal.*, 2022, **12**, 7142–7198.
12 V. Vermaak, H. C. M. Vosloo and A. J. Swarts, *Mol. Catal.*, 2021, **511**, 111738–111745.
13 E. Merino, *Chem. Soc. Rev.*, 2011, **40**, 3835–3853.
14 C. C. Hsueh, B. Y. Chen and C. Y. Yen, *J. Hazard. Mater.*, 2009, **167**, 995–1001.
15 P.-G. Rieger, H.-M. Meier, M. Gerle, U. Vogt, T. Groth and H.-J. Knackmuss, *J. Biotechnol.*, 2002, **94**, 101–123.
16 J. Fajardo and J. C. Peters, *J. Am. Chem. Soc.*, 2017, **139**, 16105–16108.
17 M. Hölscher and W. Leitner, *Chem. – Eur. J.*, 2017, **23**, 11992–12003.
18 D. Wang and D. Astruc, *Chem. Rev.*, 2015, **115**(13), 6621–6686.
19 C. Wang, C. Li, X. Wu, A. Pettman and J. Xiao, *Angew. Chem., Int. Ed.*, 2009, **48**, 6524–6528.
20 M. Ruiz-Castañeda, M. C. Carrión, L. Santos, B. R. Manzano, G. Espino and F. A. Jalón, *ChemCatChem*, 2018, **10**, 5541–5550.
21 H. W. Moon, F. Wang, K. Bhattacharyya, O. Planas, M. Leutzsch, N. Nöthling, A. A. Auer and J. Cornella, *Angew. Chem., Int. Ed.*, 2023, **62**, e202313578.
22 E. Guillamón, M. Oliva, J. Andrés, R. Llusar, E. Pedrajas, V. S. Safont, A. G. Algarra and M. G. Basallote, *ACS Catal.*, 2021, **11**, 608–614.
23 U. K. Das, S. Kar, Y. Ben-David, Y. Diskin-Posner and D. Milstein, *Adv. Synth. Catal.*, 2021, **363**, 3744–3749.
24 D. Panja, S. Dey and S. Kundu, *J. Environ. Chem. Eng.*, 2023, **11**, 109607.

25 S. Bansal, R. G. Gonnade and B. Punji, *Catal. Sci. Technol.*, 2023, **13**, 2705–2713.
26 Y. Fu and T. Viraraghavan, *Bioresour. Technol.*, 2001, **79**, 251–262.
27 S. Rafaqat, N. Ali, C. Torres and B. Rittmann, *RSC Adv.*, 2022, **12**, 17104–11713.
28 A. Toti, P. Frediani, A. Salvini, L. Rosi and C. Giolli, *J. Organomet. Chem.*, 2005, **690**, 3641–3651.
29 P. Ji, K. Manna, Z. Lin, X. Feng, A. Urban, Y. Song and W. Lin, *J. Am. Chem. Soc.*, 2017, **139**, 7004–7011.
30 D. Panja, S. Dey, R. Saha, R. Sahu, G. K. Das, P. Bhobe and S. Kundu, *Green Chem.*, 2023, **25**, 9374–9387.
31 A. Mohanty, A. Sinha, G. Kenguva, R. Dandela and P. Daw, *ChemCatChem*, 2025, **17**, e202401459.
32 H. Chai, T. Liu, D. Zheng and Z. Yu, *Organometallics*, 2017, **36**, 4268–4277.
33 T. J. Steiman and C. Uyeda, *J. Am. Chem. Soc.*, 2015, **137**, 6104–6110.
34 Y. Nishibayashi, A. Shinoda, Y. Miyake, H. Matsuzawa and M. Sato, *Angew. Chem., Int. Ed.*, 2006, **45**, 4835–4839.
35 H. F. Yuen and T. J. Marks, *Organometallics*, 2009, **28**, 2423–2440.
36 K. Fukamizu, Y. Miyake and Y. Nishibayashi, *Angew. Chem., Int. Ed.*, 2009, **48**, 2534–2537.
37 G. Deshmukh, T. R. K. Rana, N. Yadav, G. Rajaraman and R. Murugavel, *Green Chem.*, 2024, **26**, 1610–1626.
38 G. Deshmukh, S. J. Gharpure and R. Murugavel, *Organometallics*, 2024, **43**, 1190–1202.
39 G. Deshmukh and R. Murugavel, *Eur. J. Org. Chem.*, 2024, **27**, e202400131.
40 G. Deshmukh and R. Murugavel, *Synlett*, 2025, 75–78.
41 G. Deshmukh, T. R. K. Rana, G. Rajaraman and R. Murugavel, *Chem. – Asian J.*, 2025, **20**, e202401162.
42 R. Jangir, M. Ansari, D. Kaleeswaran, G. Rajaraman, M. Palaniandavar and R. Murugavel, *ACS Catal.*, 2019, **9**, 10940–10950.
43 R. Jangir, D. Kaleeswaran and R. Murugavel, *ChemistrySelect*, 2018, **3**, 8082–8094.
44 B. R. Grigg, T. R. B. Mitchell, S. Sutthivaiyakit and N. Tongpenyai, *J. Chem. Soc., Chem. Commun.*, 1981, **61**, 611–612.
45 G. Guillena, D. J. Ramón and M. Yus, *Chem. Rev.*, 2010, **110**, 1611–1641.
46 P. Wehrmann and S. Mecking, *Organometallics*, 2008, **27**, 1399–1408.
47 M. A. Bennett, T. N. Huang, T. W. Matheson, A. K. Smith, S. Ittel and W. Nickerson, *Inorg. Synth.*, 1982, **21**, 74–78.
48 *CrysAlisPRO*, Oxford Diffraction/Agilent Technol. UKLtd, Yarnton, Oxford, UK, 2014.
49 L. J. Farrugia, *J. Appl. Crystallogr.*, 2012, **45**, 849–854.
50 O. V. Dolomanov, L. J. Bourhis, R. J. Gildea, J. A. K. Howard and H. Puschmann, *J. Appl. Crystallogr.*, 2009, **42**, 339–341.
51 G. M. Sheldrick, *Acta Crystallogr., Sect. C:Struct. Chem.*, 2015, **71**, 3–8.
52 M. J. Frisch, G. W. Trucks, H. B. Schlegel, G. E. Scuseria, M. A. Robb, J. R. Cheeseman, G. Scalmani, V. Barone, G. A. Petersson, H. Nakatsuji, X. Li, M. Caricato, A. V. Marenich, J. Bloino, B. G. Janesko, R. Gomperts, B. Mennucci, H. P. Hratchian, J. V. Ortiz, A. F. Izmaylov, J. L. Sonnenberg, D. Williams-Young, F. Ding, F. Lipparini, F. Egidi, J. Goings, B. Peng, A. Petrone, T. Henderson, D. Ranasinghe, V. G. Zakrzewski, J. Gao, N. Rega, G. Zheng, W. Liang, M. Hada, M. Ehara, K. Toyota, R. Fukuda, J. Hasegawa, M. Ishida, T. Nakajima, Y. Honda, O. Kitao, H. Nakai, T. Vreven, K. Throssell, J. A. Montgomery Jr, J. E. Peralta, F. Ogliaro, M. J. Bearpark, J. J. Heyd, E. N. Brothers, K. N. Kudin, V. N. Staroverov, T. A. Keith, R. Kobayashi, J. Normand, K. Raghavachari, A. P. Rendell, J. C. Burant, S. S. Iyengar, J. Tomasi, M. Cossi, J. M. Millam, M. Klene, C. Adamo, R. Cammi, J. W. Ochterski, R. L. Martin, K. Morokuma, O. Farkas, J. B. Foresman and D. J. Fox, *Gaussian 16, Revision C.01*, Gaussian, Inc., *Wallingford CT*, 2016.
53 R. Ditchfield, W. J. Hehre and J. A. Pople, *J. Chem. Phys.*, 1971, **54**, 720–723.
54 F. Weigend and R. Ahlrichs, *Phys. Chem. Chem. Phys.*, 2005, **7**, 3297–3305.
55 J. Tomasi, B. Mennucci and R. Cammi, *Chem. Rev.*, 2005, **105**, 2999–3093.
56 E. D. Glendening, C. R. Landis and F. Weinhold, *J. Comput. Chem.*, 2013, **34**, 1429–1437.
57 (*a*) G. Deshmukh, T. R. K. Rana, N. Yadav, G. Rajaraman and R. Murugavel, CCDC 2432945: Experimental Crystal Structure Determination, 2025, DOI: **10.5517/ccdc.csd.cc2mnp33**; (*b*) G. Deshmukh, T. R. K. Rana, N. Yadav, G. Rajaraman and R. Murugavel, CCDC 2432946: Experimental Crystal Structure Determination, 2025, DOI: **10.5517/ccdc.csd.cc2mnp44**; (*c*) G. Deshmukh, T. R. K. Rana, N. Yadav, G. Rajaraman and R. Murugavel, CCDC 2432947: Experimental Crystal Structure Determination, 2025, DOI: **10.5517/ccdc.csd.cc2mnp55**; (*d*) G. Deshmukh, T. R. K. Rana, N. Yadav, G. Rajaraman and R. Murugavel, CCDC 2432948: Experimental Crystal Structure Determination, 2025, DOI: **10.5517/ccdc.csd.cc2mnp66**.